A novel method for estimating three-dimensional patellofemoral kinematics using optical motion capture with a knee marker grid, and a shape fitting algorithm.

By Lonit Peeters

5126533

Master Thesis BioMechanical Design

Department of Biomechanical Engineering

Faculty of Mechanical, Maritime, and Material Engineering

Delft University of Technology

To be defended publicly on June 6th, 2024

Course code	ME51035	
Period	July 2023 – June 2024	
Thesis committee	Prof.dr.ir. J. Harlaar	TU Delft, chair
	Dr. M.G.H. Wesseling	TU Delft, supervisor
	A. Seth	TU Delft, independent assessor

Electronic version available at http://repository.tudelft.nl

TU Delft

Abstract

Background: Abnormal patellofemoral joint loading patterns may cause patellofemoral pain and may be caused by patellar maltracking. Treatment is aimed at restoring normative patellofemoral kinematics. For this, an accurate estimation of the patellofemoral kinematics is necessary. While 4-dimensional computed tomography (4D-CT) can provide this by capturing bone geometries, this equipment is not commonly available in clinical settings and requires radiation. Optical Motion Capture (OMC) with a grid of markers overlying the bone has shown promising results for measuring scapular and patellofemoral kinematics.

Objective: The aim of this study is to develop and validate a new method to estimate patellofemoral kinematics from OMC by applying a shape fitting algorithm to a knee marker grid.

Methods: Five participants were equipped with a knee marker grid and performed a prone extension-flexion movement during which kinematics were measured using OMC and 4D-CT. Patellofemoral kinematics were estimated using three methods: *Geometry-based 4D-CT*, *Grid-based 4D-CT*, and *Grid-based OMC*. In Geometry-based 4D-CT, PF kinematics were obtained from bone geometries. In both Grid-based methods, a shape fitting algorithm using an Iterative Closest Point algorithm estimated the patellofemoral kinematics from the locations of the grid markers. For validation, both 4D-CT methods were compared, as well as both Grid-based methods. To quantify the validity of the new method, root mean square errors (RMSEs) of the differences between the methods and Spearman correlation coefficients were computed.

Results: For *Geometry-based 4D-CT* vs. *Grid-based 4D-CT*, the RMSEs of the differences were 7° for flexion and 3 to 10 mm for all translations, combined with very high correlations. The RMSEs for tilt and spin were over 18°, combined with low and moderate negative correlations. For *Grid-based 4D-CT* vs. *Grid-based OMC*, RMSEs were smallest for ML translation (4 mm) and spin and tilt (< 6°), but these were paired with moderate correlations. On the other hand, the higher RMSEs for flexion (9°) and AP and SI translation (> 10 mm) were paired with moderate to very high correlations.

Conclusion: Comparing the 4D-CT methods indicated that spin and tilt could not be measured accurately using the marker grid, which are both clinical relevant. Comparing the Grid-based methods showed large differences between OMC and 4D-CT, probably introduced by the accuracy of the measurement system. Overall, the shape fitting algorithm thus seems to be able to estimate PF flexion and all three PF translations from a marker grid, but applying it to OMC data is not valid yet.

Table of contents

List of abbreviations

Abbreviation	Definition
3D	3-dimensional
3D-CT	3-dimensional computed tomography
4D-CT	4-dimensional computed tomography
ACS	Anatomical coordinate system
AP	Anterior-posterior
CT	Computed tomography
DoF	Degree of freedom
EF	Extension-flexion
ICP	Iterative Closest Point
ML	Medial-lateral
OMC	Optical motion capture
PF	Patellofemoral
PFOA	Patellofemoral osteoarthritis
PFP	Patellofemoral pain
RMSE	Root mean square error
SI	Superior-inferior
STA	Soft tissue artefact
TF	Tibiofemoral

1 Introduction

Patellofemoral pain (PFP) is one of the most common forms of knee pain (Smith et al., 2018). It is described as non-traumatic diffuse knee pain that is aggravated during joint-loading activities such as squatting, running, or stair climbing (Crossley et al., 2016; Smith et al., 2018). The annual prevalence of PFP is over 20% in the general population and almost 30% in adolescents (Smith et al., 2018). Combined with this high prevalence, PFP is associated with a reduced ability to perform sports, physical activity, and work-related activities (Crossley et al., 2016) and a lower quality of life (Coburn et al., 2018). Furthermore, patellofemoral osteoarthritis (PFOA) may be related to PFP (Wyndow et al., 2016). For example, patients with chronic PFP often show radiographic PFOA or develop it on the long term (Thorstensson et al., 2009). Moreover, patients undergoing surgery for isolated PFOA often report having had PFP as an adolescent, unlike patients undergoing surgery tibiofemoral osteoarthritis (Utting et al., 2005).

PFP may be caused by abnormal patellofemoral (PF) joint loading patterns and elevated cartilage stress (Powers et al., 2017; Wheatley et al., 2020). Joint loading and stress are determined by the forces that the patella and femur exert on each other, and are thus influenced by the 6 degree of freedom (DoF) PF kinematics: the 3-dimentional (3D) movement of the patella with respect to the femur (Figure 1). Abnormal loading patterns may be caused by abnormal PF kinematics, such as excessive lateral tilt (Powers et al., 2017; Wheatley et al., 2020). Furthermore, abnormal PF kinematics have been shown to be related to both PFP and PFOA (Drew et al., 2016; Macri et al., 2016; Petersen et al., 2014; Tsavalas et al., 2012). Therefore, PFP treatment often aims to improve patellar kinematics (Fick et al., 2022), for which an accurate estimation of patellar kinematics is necessary. Since the pain in PFP occurs mostly during weight-bearing activities, measuring patellar kinematics during functional weight-bearing tasks would provide most clinically useful information.

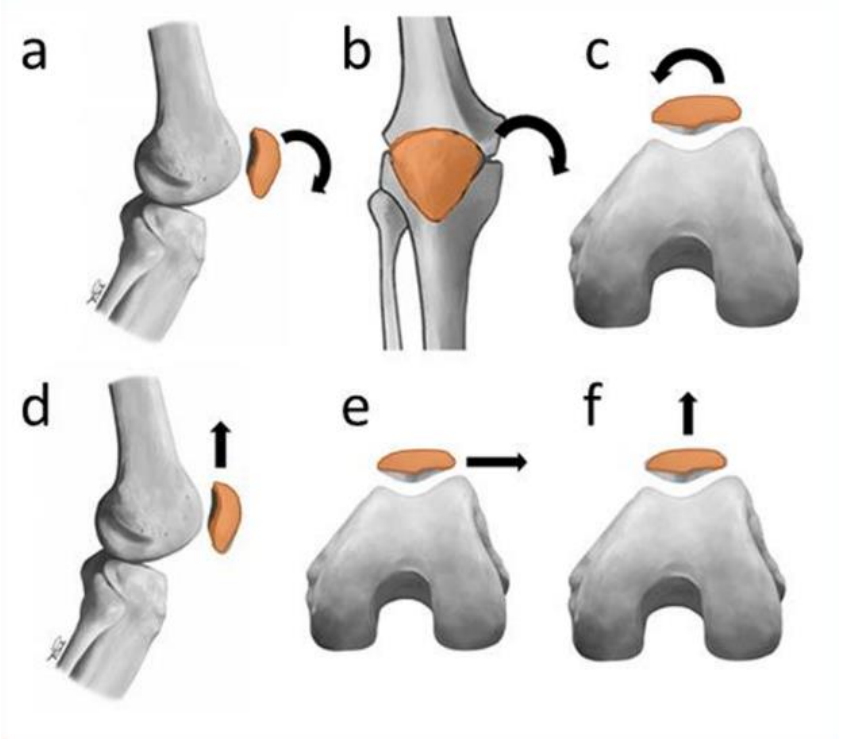

Figure 1: 6DoF patellar kinematics; a) flexion/extension, b) spin, c) tilt, d) superior-inferior (SI) translation, e) medial-lateral (ML) translation, f) (AP) anterior-posterior translation. Modified from illustrations by Vicky Earle, reprinted with permission from (Macri, 1997).

To measure patellofemoral kinematics during functional weight-bearing tasks, several methods are currently being used, including ultrasound, kinematic magnetic resonance imaging (MRI), and single-plane and biplane fluoroscopy (Wheatley et al., 2020; Yu et al., 2019). Of those, fluoroscopy appears to be the most valid and reliable, but its clinical feasibility might be lower due to radiation exposure and the availability and costs of the required equipment (Peeters et al., 2024). Therefore, there is a need for a valid and reliable method avoiding these drawbacks.

A commonly used method for measuring bony movements in functional weight-bearing tasks is optical motion capture (OMC). In OMC, the motion of markers attached to the skin on top of bony landmarks is measured in order to estimate the bony movements. Although this method works well for some bony movements, it is very sensitive to soft tissue artefacts (STAs) – movement of the skin mounted markers relative to the underlying bones – especially during and just after impact. Maximum errors in tibiofemoral (TF) kinematics due to STAs have been shown to be up to 7° and 10 mm before impact and up to 15° and 28mm after impact in a jump-cut task (Miranda et al., 2013).

Since the patella moves largely relative to the overlying skin and soft tissue during motion (Akbarshahi et al., 2010), OMC is certainly not suitable for measuring PF kinematics. Yet, OMC has been used to measure kinematics of the scapula, a bone that also moves relative to the skin and soft tissue, not using dedicated markers but by placing a grid of small markers on the skin overlying the scapula (Charbonnier et al., 2014; Mattson et al., 2012). The idea was that the shape of the scapula would reflect in the deformation of the grid. A preliminary study found that the shape of the patella was also visible in the deformation of an interpolated marker grid and that this visible shape could be used to estimate PF translations in flexed knees (error < 5 mm) (Zandee, 2022). Furthermore, the shape of the patella could be extracted from 3D point cloud data of the knee (Oh & Kim, 2017). Fitting a known patellar shape onto an (interpolated) marker grid might help to also estimate PF rotations and PF translations in extended knees. For example, Inai et al. (2020) fitted the shape of the patella onto a marker grid, which was measured using computed tomography (CT) in static knee flexion angles. They did this by minimizing the difference between the vertical distance of each triangle in the patella mesh to the skin and the vertical distance of each triangle in the patella mesh to its closest grid marker, where the vertical distance was parallel to the normal vector of the triangle. This resulted in errors of up to 10 mm and 10° for the static PF kinematics. However, there was no mention of minimizing the horizontal distance between the marker and the triangles of the patella mesh. Furthermore, the distances between the patella mesh and the skin had to be measured using CT, limiting the usefulness of this fitting algorithm.

The aim of this study is to develop and validate a method to measure 6 DoF PF kinematics in functional weight-bearing tasks using OMC with a knee marker grid, and a shape fitting algorithm. For validation, the results will be compared to 4-dimensional CT (4D-CT), which has been shown to be able to accurately measure PF kinematics over time (Wong et al., 2022). Using 4D-CT, PF kinematics will be obtained from bone geometries (Geometry-based 4D-CT) and estimated from a knee marker grid (Grid-based 4D-CT). Furthermore, PF kinematics will be estimated from a knee marker grid measured with OMC (Grid-based OMC). Using these different methods to estimate the PF kinematics, the following questions will be answered:

a. *Geometry-based 4D-CT vs. Grid-based 4D-CT*: To what extent do 6DoF PF kinematics estimated from a knee marker grid agree to those obtained from bone geometries, both measured using 4D-CT?
b. *Grid-based 4D-CT vs. Geometry-based OMC*: To what extent do 6DoF PF kinematics estimated from a knee marker grid differ when measured using 4D-CT or OMC?

As a further validation, the influence of STAs of the femur markers and the definition of the femur Anatomical Coordinate System (ACS) on the estimated PF kinematics will be investigated. For this, the movement of the femur ACS will be estimated from bone geometries and from femur markers, both measured using 4D-CT. This will answer the following question:

c. To what extent do femur kinematics estimated from femur markers differ from those obtained from bone geometries, both measured using 4D-CT?

2 Methods

2.1 Participants

Five healthy, young adults (4F, 1M) were included (age: 23.4 ± 2.3 years, BMI: 21.9 ± 2.1 kg/m^2). Exclusion criteria were (history of) neurological and rheumatic conditions, musculoskeletal injuries or pain in the lower extremity of the dominant leg, pregnancy, cancer treatment, and contraindications to radiation exposure. Ethical approval was obtained from the institutional review board of the Erasmus Medical Centre (NL76580.078.21), and all participants gave their written informed consent.

2.2 Optical motion capture

Participants were equipped with six spherical retro-reflective markers (diameter 19 mm) on the tibia and femur. The tibia markers were attached on the lateral and medial malleolus (LM and MM marker) and on the lateral tibia plateau (LTP marker) (Figure 3; Appendix A). The femur markers were attached on the lateral and medial epicondyle (LEC and MEC marker), and on a point superior to the LEC marker, but inferior to the belly of the vastus lateralis (FEXTRA marker; Figure 4). Furthermore, 49 smaller spherical retro-reflective markers (diameter 4 mm) were attached to the skin of the knee of the dominant leg (right leg for all participants) (Figure 4). The markers were placed at horizontal and vertical distances of approximately 2 cm (for participants 1 and 2) or 1.75 cm (for participants 3, 4, and 5), forming a grid of 7 x 7 markers covering the skin area overlaying the patellar range of motion. The locations of the 49 grid markers and the 3 femur markers were drawn on the skin using permanent marker before attaching the markers to the skin. A 12-camera OMC system (Qualisys AB, Göteborg, Sweden) recorded the 3D positions of the retro-reflective markers (100 Hz). Of those 12 cameras, 3 were removed from their usual attachment and placed on the ground facing slightly upwards (Figure 2). This was needed to be able to measure the small grid markers during the movement task as described below.

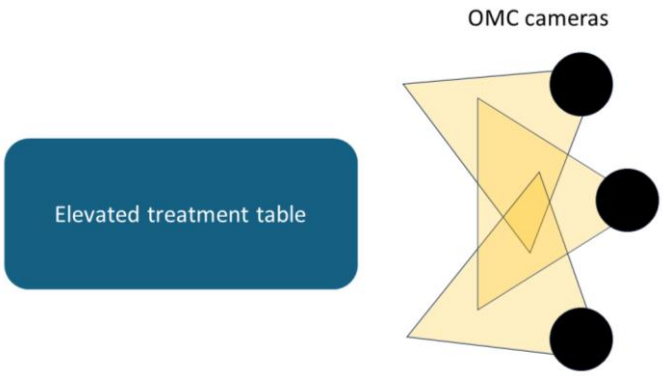

Figure 2: Set up of the three OMC cameras placed on the ground and the elevated treatment table.

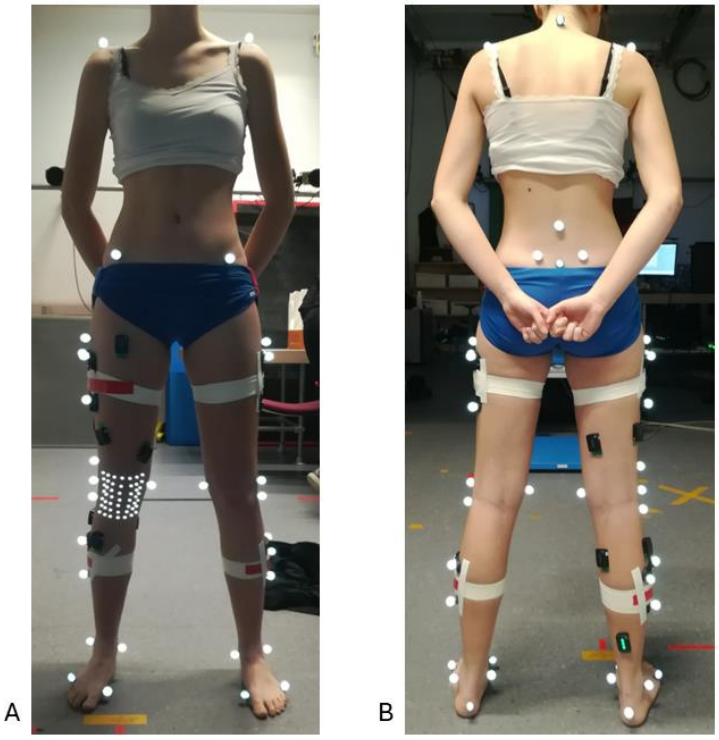

Figure 3: Picture of the placement of all markers, marker clusters, and the EMG sensors (Appendix B) for one participant.

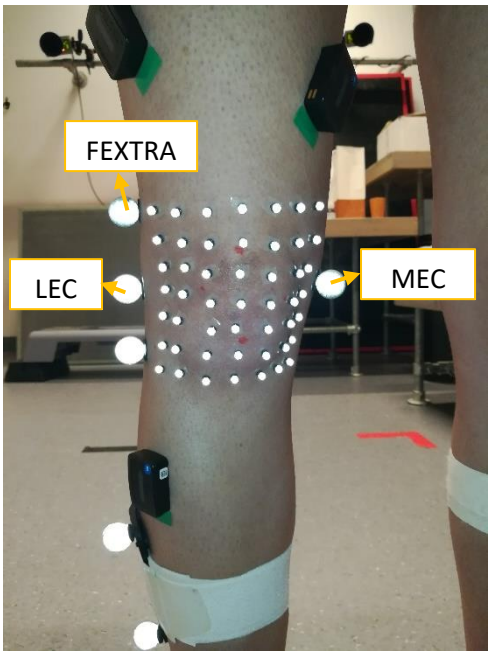

Figure 4: Picture of the knee marker grid and the femur markers for one participant.

Participants were asked to perform a prone extension-flexion movement (EF). The participants lay on their belly on an elevated treatment table with their knees hanging over the edge. The nondominant leg was held in a flexed position to avoid obstruction of the markers on the dominant leg. While watching an instruction video showing the required speed, the participants slowly flexed their knee from full extension to about 70° of knee flexion in 8 seconds. The participants were allowed to

practice this movement until they felt comfortable. Then, the participant performed the EF movement three times.

Additional data was collected but was not used in this study. This additional data consisted of more retro-reflective markers, other tasks, and other types of data (e.g. EMG) (Appendix B).

2.3 CT scanning

Prior to scanning, 3 large markers (diameter 19 mm) and the 49 small markers (diameter 4 mm) were attached to the skin of the femur and knee on the same locations as during OMC, using the drawn locations (Figure 4). A static 3D-CT scan was made while the participant was lying prone in the CT scanner (TSX-301A-Aquilion ONE, Canon Medical Systems, Otawara, Japan) with their knee hanging over the edge of the scanning bed. The participants were instructed to perform the same EF as during OMC, but now with both legs simultaneously. The same instruction video was played during the scan and participants could again practice the movement until they felt comfortable. During the EF, dynamic 4D-CT scans were made at a sample rate of 2 Hz, which resulted in 21 dynamic 4D-CT scans. The settings for the static 3D-CT and the dynamic 4D-CT scans differed and can be found in Table 1.

Table 1: CT settings for the static and dynamic scans

	Static 3D-CT	**Dynamic 4D-CT**
Field of view (mm)	285.6-320	160
Matrix size	512 x 512	512 x 512
Slice thickness (mm)	1.0	0.5
Increment (mm)	0.8	0.5
Pixel spacing (mm)	0.782	0.782
Spiral Pitch Factor (-)	0.813	-
Peak potential (kV)	120	100
Radiation time (s)	0.500	0.350
Number of scans (-)	1	21
Total scanning time (s)	-	10
$CTDI_{vol}$ (mGy)	2.4	40.60
Radiation exposure (mAs)	20	35

2.4 Calculation of PF kinematics

An algorithm was developed that fits a patellar shape to the knee grid to estimate PF kinematics from a knee marker grid. To validate this algorithm and answer the first two research questions (see *Introduction*), PF kinematics were computed in four ways, using either OMC or 4D-CT data, and based on either marker grid data or knee geometry obtained from CT (Table 2). Furthermore, TF kinematics were computed to be able to compare the PF kinematics over the different methods, and femur kinematics were computed to answer the third question (see *Introduction*).

Table 2: Summary of the comparisons to answer the research questions and validate the method. The differences in each comparison are highlighted.

Question	Comparison	Method	Source of ACS			
			Patella	**Femur for PF**	**Femur for TF flexion**	**Tibia**
a.	Geometry-based 4D-CT	4D-CT	Geometry	Geometry	Geometry	Geometry
	Grid-based 4D-CT	4D-CT	Geometry fitted on marker grid	Geometry	Geometry	Geometry
b.	Grid-based 4D-CT	4D-CT	Geometry fitted on marker grid	Markers	Geometry	Geometry
	Grid-based OMC	OMC	Geometry fitted on marker grid	Markers	Marker	Marker
c.	Geometry-based femur ACS	4D-CT	-	Geometry	Geometry	Geometry
	Marker-based femur ACS	4D-CT	-	Markers	Geometry	Geometry

2.4.1 Geometry-based 4D-CT

We used an improved version of the semi-automated workflow developed by Oosterbaan (2023), available on Gitlab[1], to compute patellofemoral kinematics (see Appendix C for an overview of all scripts, and Appendix D for an overview of the improvements to the code). In this workflow, the 4D-CT scans were first segmented in 3D Slicer version 5.0.3 (Fedorov et al., 2012) to obtain 3D surface models of the bones. The static bone models were then registered to the dynamic bone models using Python. Next, the anatomical coordinate systems were determined using the algorithm by Chen et al. (2020) in MATLAB (MathWorks, 2021) (Figure 5). Finally, the patellofemoral and tibiofemoral kinematics were defined as the rotation and translation of the patellar ACS with respect to the femoral ACS, and the rotation and translation of the tibial ACS with respect to the femoral ACS, respectively.

[1] https://gitlab.tudelft.nl/clinical-biomechanical-lab/4d-ct-knee-kinematics/-/tree/Lonit?ref_type=heads

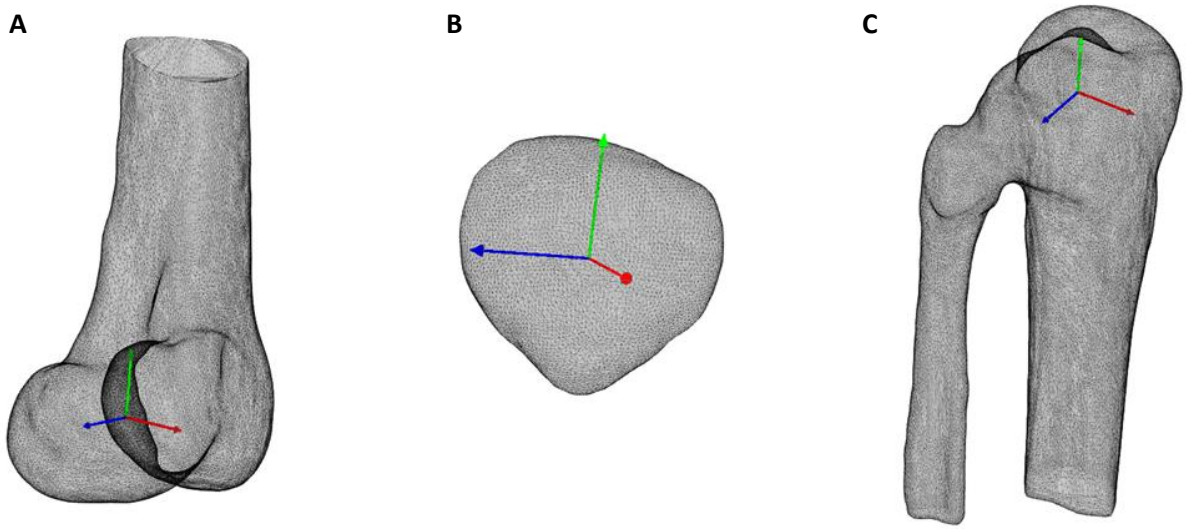

Figure 5: ACSs for femur (A), patella (B), and tibia (C), as determined by the algorithm of Chen et al. (2020). The x-, y, and z-axis are printed in respectively red, green, and blue. For all bones, the x-axis was in the AP direction, the y-axis in the SI direction, and the z-axis in the ML direction, pointing to the right. For the femur, first two cylinders were fitted to the condyles and a line was created that connected the projections of the articulating surfaces of the condyles onto the cylinder axis. The origin was then defined as the middle of this line. The ML-axis was along this line, the AP-axis was perpendicular to the ML-axis and the third inertial axis of the femur, and the SI-axis was perpendicular to the ML- and AP-axis. For the patella, the origin was defined as the centroid, the AP-axis was normal to the anterior surface, the SI-axis connected the origin to the most inferior point, and the ML-axis was perpendicular to the AP- and SI-axis. For the tibia, first the tibial plateau is cut off at the maximum cross-sectional area along the third inertial axis. The origin is defined as the centre of mass of the plateau, and the inertial axes of the plateau form the AP-, SI-, and ML-axis.

2.4.2 Grid-based 4D-CT

For the segmentation of the CT scans, we developed a semi-automated workflow based on Oosterbaan (2023). Artefacts (small segments identified as bony material but not connected to the bones) could not be removed automatically since these had a similar size as the grid markers, therefore we chose to add a manual step in which artefacts and bones were removed manually from the initial segmentation. In this manual step, we were also able to check for scans in which markers were not identified due to blurring in fast movements. This blurring influences the grey value in the CT scan, which is used by the algorithm to distinguish the bones and markers from the soft tissues. Furthermore, in two scans, one marker was not identified while being visible on the scan, so we decided to add this marker by manually segmenting it from the scans. Since we were unable to write a script to label the femur markers and the corner markers of the grid, marker labelling also needed to be done in the manual step. After the manual step, a sphere was fit to the all knee grid markers and all femur markers using Trimesh version 4.1.8 (Dawson-Haggerty, 2023). The centres of these spheres were then input to the *Shape-Fitting Algorithm* described below to compute the patella ACS.

To limit the number of factors causing potential differences, the femur ACS was computed using two different methods within Grid-based 4D-CT (Table 2). For the comparison of Grid-based 4D-CT and Geometry-based 4D-CT, the femur ACS was computed based on the geometry using the algorithm of Chen et al. (2020) (Figure 5). For the comparison of Grid-based 4D-CT and Grid-based OMC, the femur ACS was computed from the locations of the femur markers (Figure 6A). The patellofemoral and tibiofemoral kinematics were defined the same way as for Geometry-based 4D-CT.

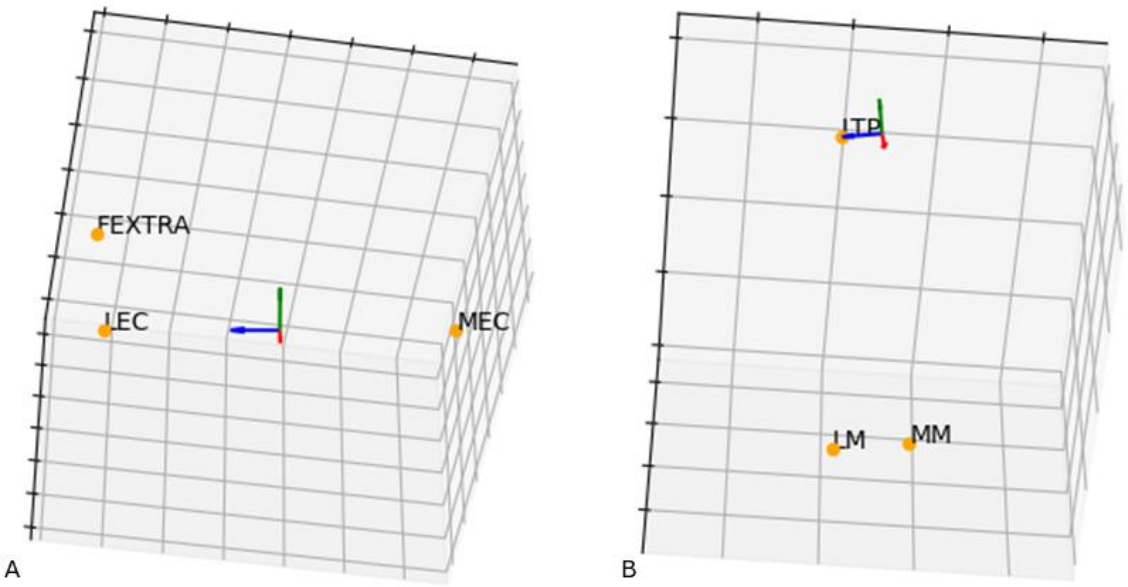

Figure 6: Definition of the femur ACS based on the MEC, LEC, and FEXTRA marker and the tibia ACS based on the LTP, LM, and MM marker. Similarly to the algorithm of Chen et al. (2020), the x-axis was in the AP direction, the y-axis in the SI direction, and the z-axis in the ML direction, pointing to the right. (A) For the femur, the origin was defined as the middle between the MEC and the LEC marker. The ML-axis was along the line between the MEC and the LEC marker. A temporary SI-axis was defined as being parallel to the line between the LEC and the FEXTRA marker, pointing superiorly. The AP-axis was then perpendicular to the ML-axis and the temporary SI-axis. The final SI-axis was again perpendicular to the ML-axis and the AP-axis. (B) For the tibia, a temporary origin was constructed in the middle between the MM and LM marker. The ML-axis was along the line between the MM and the LM marker. A temporary SI-axis was defined as being parallel to the line between the LM and the LTP marker, pointing superiorly. The AP-axis was then perpendicular to the ML-axis and the temporary SI-axis. The final SI-axis was again perpendicular to the ML-axis and the AP-axis. The final origin was constructed by translating the temporary over the SI-axis by the same distance as the distance between the LM and LTP axis.

2.4.3 Grid-based OMC

Markers were labelled using an Automatic Identification of Markers (AIM) model in Qualysis Track Manager version 2023.2 (Qualysis, 2020). Small gaps in the marker trajectories (≤ 20 frames, i.e. 200 ms) were filled using the inbuild Gap-Filling function with a polynomial fill type. This fill type uses interpolation to smoothly fill the gaps in the x-, y, and z-coordinates of a marker. When marker data was missing at the start or end of the movement, that part of the movement was excluded. Trials with large gaps in the marker trajectories were excluded. Finally, grid marker positions were extracted at steps of 500 ms (same step size as in 4D-CT, Table 1) and input to the *Shape-Fitting Algorithm* described below to compute the patella ACS.

Femur marker positions were extracted and used to compute the femur ACS in the same way as for Grid-based 4D-CT (Figure 6A). Similarly, tibia marker positions were extracted and used to compute the tibia ACS (Figure 6B). The patellofemoral and tibiofemoral kinematics were defined the same way as for Grid-based 4D-CT.

2.4.4 Shape-Fitting Algorithm

A local coordinate system of the marker grid was constructed with the origin in the most distal-medial marker, the x-axis through the most distal-lateral marker, the z-axis perpendicular to the plane defined by the x-axis and the most proximal-medial marker, pointing anteriorly, and the y-axis

perpendicular to the x-axis and z-axis (Figure 7). Next, the grid marker locations were interpolated to get the location of virtual markers at a 1 mm grid, resulting in on average around 13,000 virtual markers for participants 1 and 2, and around 9,500 virtual markers for participants 3, 4, and 5. The amount of virtual markers was larger for participants 1 and 2 because the distance between the measured markers was larger for those participants and the interpolation was based on distance between virtual markers.

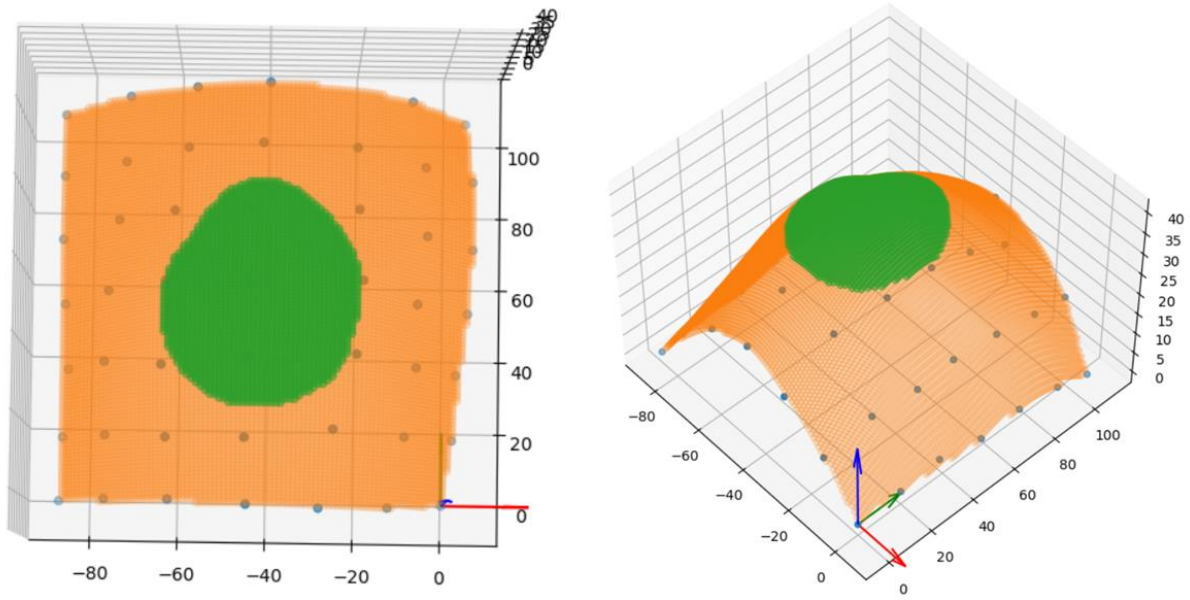

Figure 7: Measured marker grid (blue dots) together with its local CS (arrows), the virtual marker grid (orange dots), and the virtual markers selected for the registration of the patella (green dots); (A) anterior view to see the shape of the selected virtual markers, and (B) view to see the local CS with the x-, y, and z-axis printed in respectively red, green, and blue.

An Iterative Closest Point (ICP) algorithm was used to estimate the location and orientation of a patella mesh relative to the virtual marker grid. An ICP algorithm is an algorithm that aims to find the location and orientation of point cloud A that minimizes the cost function describing the distance between point cloud A and point cloud B (Besl & McKay, 1992). The lower the final cost, the better is the fit between the two point clouds.

In the shape fitting algorithm, the aim is to fit a patella mesh onto the virtual marker grid. The participant-specific patella from the static CT scan was used as patella mesh for each participant. Since only the anterior part of the patella protrudes through the skin, the anterior surface of the patella mesh was selected as all faces within a certain distance of the most anterior face on the patella. This distance was visually determined for each participant as being 1/4 or 1/5 of the size of the patella in AP direction (determined using inertial axes; Figure 8). The anterior surface of the patella mesh was then inputted into the ICP algorithm from Trimesh version 4.1.8 (Dawson-Haggerty, 2023). The cost in the ICP algorithm was computed as the mean squared distance of the points of the anterior part of the patella mesh to the selected virtual markers.

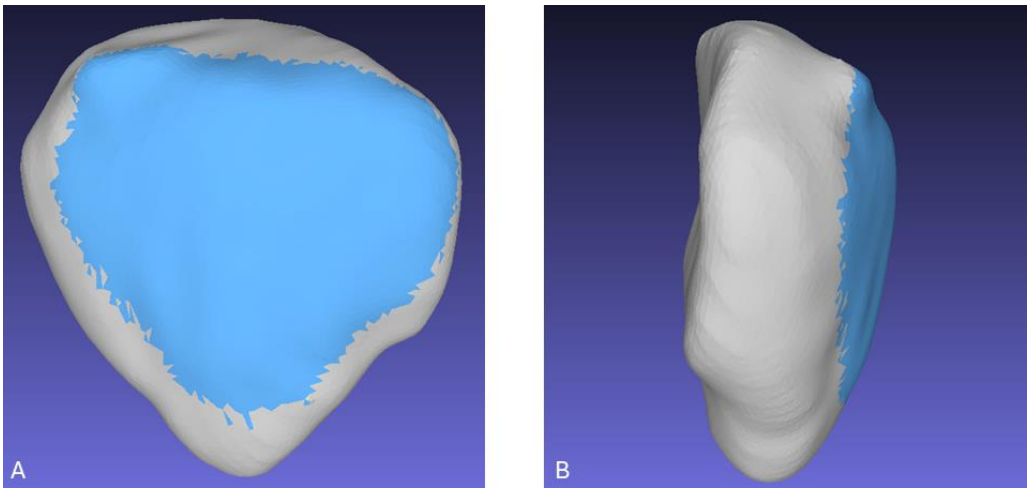

Figure 8: Visualisation of the anterior surface of the patella that was input for the Iterative Closest Point (ICP) algorithm for one participant.

To improve the fit on the virtual marker grid, a multiple of 100 virtual markers with the highest z-values was selected, such that the width of the selected region was 4 mm larger than the width of the selected anterior surface of the patella mesh (Figure 7, Figure 9). This idea was based on a preliminary study that was able to estimate the translations of the patella by selecting a certain number of virtual markers as being the patella (Zandee, 2022). As an initial guess, the AP-axis of the patella (determined using inertial axes) was first aligned with the z-axis of the marker grid. Then, the patella mesh was translated such that the x- and y-coordinate of the centre of the full mesh coincided with the x- and y-coordinate of the centre of the selected part of the grid, and the most anterior point of the patella mesh coincided with the z-coordinate of the centre of the selected part of the grid.

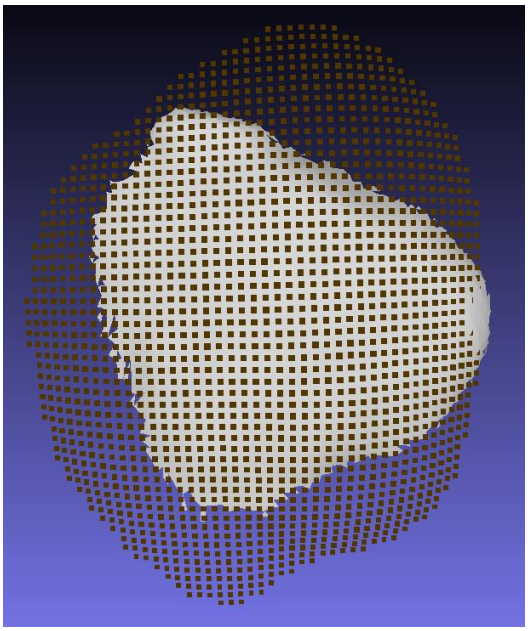

Figure 9: Initial guess of the anterior surface of the patella mesh together with the selected virtual markers for one scan of one participant.

The ICP algorithm was then performed without scaling to fit the anterior surface of the patella mesh onto the selected part of the virtual marker grid. To fit the full patella mesh onto the selected part of the virtual marker grid, the full patella mesh was transformed such that it coincided with the cut mesh. To compute the dynamic patella ACS, the ACS of the patella mesh was first computed from the static CT scan using the algorithm of Chen et al. (2020). The rotations and translations for the initial guess were first applied to this ACS, then it was multiplied with the transformation matrix that resulted from the ICP algorithm.

It was attempted to adapt the algorithm such that it uses the result of the previous TF flexion angle (starting with the highest knee flexion) as an initial guess (coupled initial guess). However, since the coordinate system of the virtual grid markers changes for each scan, this initial guess was in the wrong coordinate system. Therefore, it was unclear whether the initial coupled guess has a rotation and orientation close to the actual rotation and orientation, and it was decided not to use this method in the final algorithm. However, some interesting results were observed during the process of creating this, these can be found in Appendix F.

2.5 Data analyses

Patellofemoral rotations and translations were computed for all methods and plotted against TF flexion angle. Root mean square errors (RMSEs) of the difference between *Geometry-Based 4D-CT* and *Grid-Based 4D-CT* and of the difference between *Grid-Based 4D-CT* and *Grid-Based OMC* were computed for all tibiofemoral flexion angles. Bland-Altman plots were created to compare the errors between *Geometry-Based 4D-CT* and *Grid-Based 4D-CT*, and between *Grid-Based 4D-CT* and *Grid-Based OMC*. Spearman correlation coefficients (r) were computed and interpreted as low ($r < 0.35$), moderate (r 0.36-0.67), high (r 0.68-0.90), or very high ($r > 0.90$) (Taylor, 1990).

Global rotations and translations of the femur ACS computed from bone geometries and femur markers were computed and plotted against geometry-based TF flexion angle. Furthermore, the relative rotations and translations of the geometry-based femur ACS with respect to the marker-based femur ACS were computed and plotted against geometry-based TF flexion angle.

All analyses were also performed including only the data for TF flexion angles of 20° and higher. The patella engages in the trochlea for TF flexion angles of 20° and higher (Colvin & West, 2008), while for low TF flexion angles, the patella lies superior of the trochlear groove. Furthermore, in extended knees, the skin covering the patella is loose. Combined, this causes the patella to protrude less through the skin for extended knees (TF flexion < 20°) than for flexed knees (TF flexion > 20°), which might introduce additional difficulties in estimating the position and orientation of the patella.

3 Results

3.1 Measurements

Some scans in the 4D-CT measurements had to be excluded due to missing data. For one participant, the anterior lateral knee marker moved out of the scanning window during the EF movement, becoming invisible in the last six 4D-CT scans. For another participant, the anterior lateral knee marker was out of the scanning window for the full 4D-CT measurement. We included these scans in the comparison of *Geometry-based 4D-CT* with *Grid-based 4D-CT*, since the femur ACS is based on the femur geometry in this comparison. However, we excluded these scans for the comparison of *Grid-based 4D-CT* with *Grid-based OMC*, since the femur ACS is based on the femur markers in this comparison. Furthermore, three participants had missing grid markers and clearly visible movement artefacts in the last scans of their 4D-CT measurement (two, one, and three scans for respectively participant 1, 4, and 5). This was caused by the fast extension movements those participants made after finishing the slow EF movement. These scans were excluded in the rest of the algorithm. Finally, participant 2 had one scan with missing grid markers halfway during the EF motion, this scan was also excluded in the rest of the algorithm.

In several OMC trials, some grid or knee markers were invisible during part of the trial, causing gaps in the position data. For participant 1, all three trials contained a large gap in the data for one or more grid markers at the start of the measurement. However, the rest of the measurement (containing most of the EF movement) could be used for analysis. For participant 2, one trial contained both a large gap at the start and end of the measurement, making it not useful for the analysis. The other two trials did not contain large gaps. For participant 4, one grid marker was invisible during one full measurement and there were large gaps in the data for the LEC marker in the other two measurements. It was decided to interpolate the data for the missing grid marker (which was at the edge of the marker grid) to be able to include at least one trial for this participant.

Since the pattern of the TF flexion angle was similar over the OMC trials, only one OMC trial was included for each participant (Figure 10). The trial with the largest excursion in TF flexion was included since this trial contains most information.

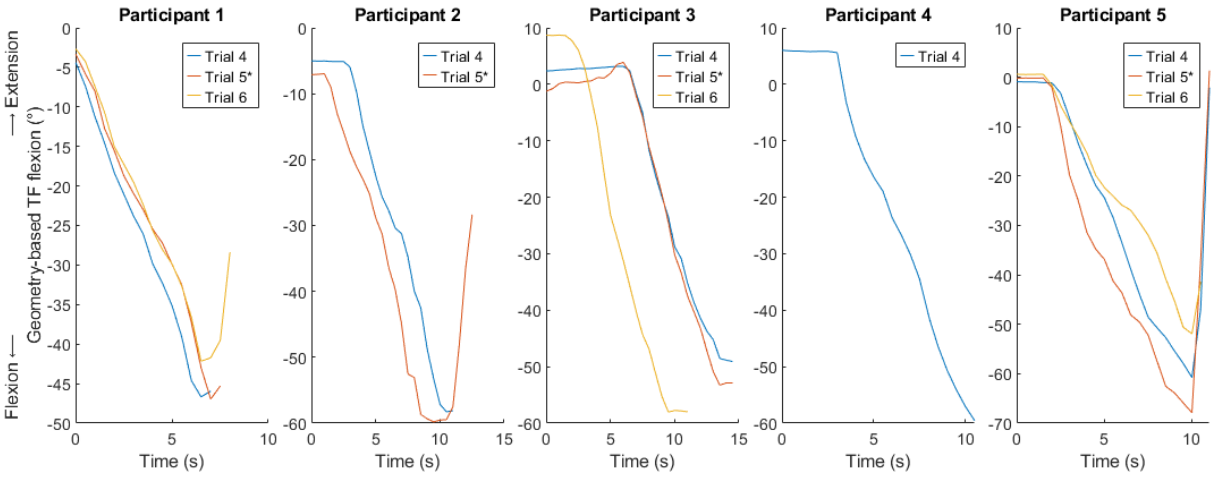

Figure 10: TF flexion angle measured using OMC for all participants and all trials. Each colour represents a different trial. The trial with the largest excursion is indicated with an asterisk (*).

3.2 Geometry-Based 4D-CT vs. Grid-Based 4D-CT

Large differences between participant 2 and the other four participants were present for *Grid-Based 4D-CT*, especially for spin and tilt (Figure 11).

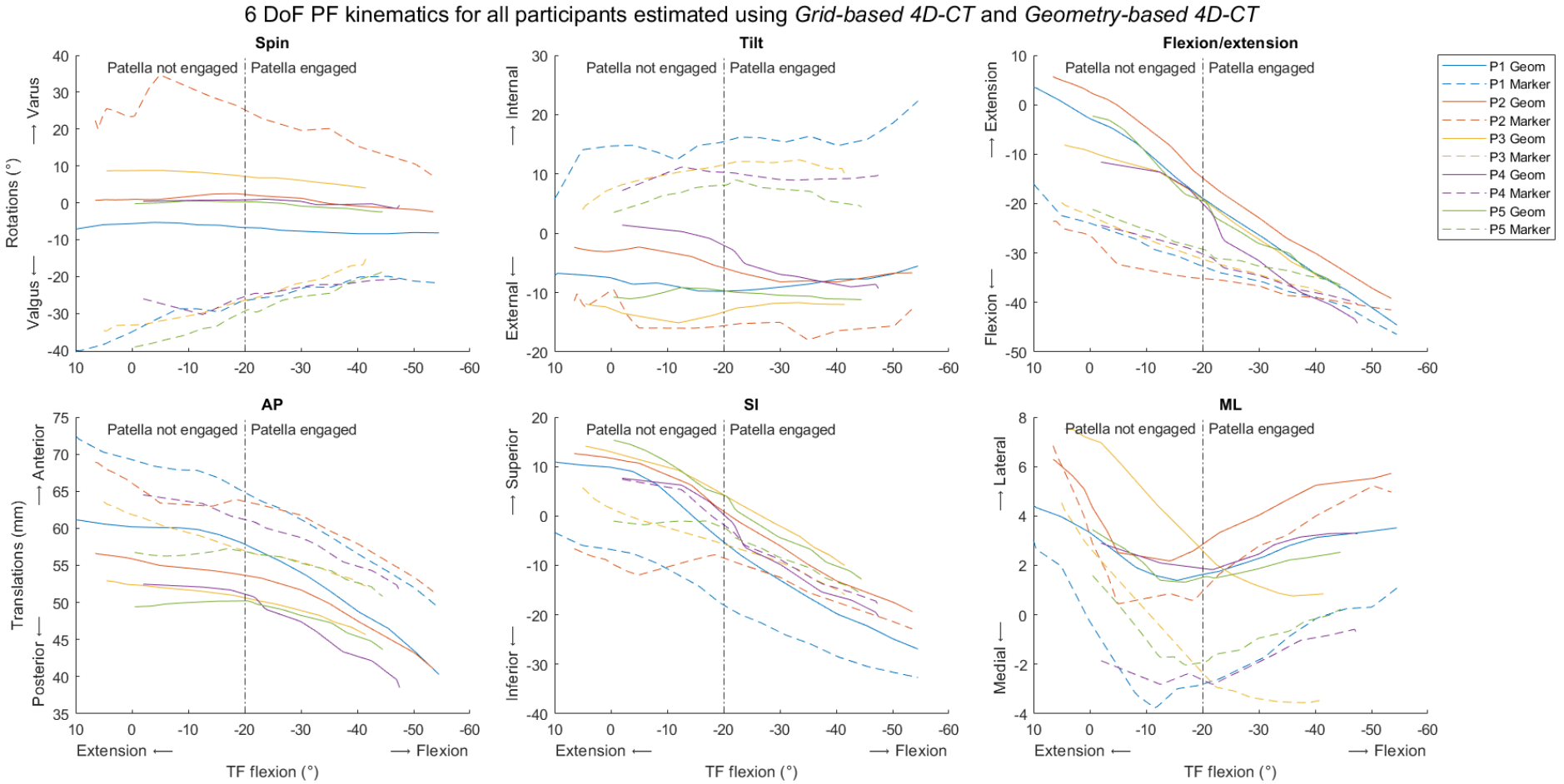

Figure 11: PF kinematics of all participants for Geometry-Based 4D-CT vs. Grid-Based 4D-CT. TF flexion angle is computed from tibial and femoral geometry for both methods. Each colour represents a different participant.

Average RMSEs of the differences between the methods were less than 10 mm and up to 27° for the comparison of *Geometry-Based 4D-CT* and *Grid-Based 4D-CT* (Table 3). The smallest differences were observed for ML translation (mean RMSE 3.3 mm). Average correlations were very high for all translations, moderate for flexion, low for tilt, and moderate negative for spin.

For the angles in which the patella is engaged (TF flexion angle larger than 20°), the average RMSEs of the differences between the methods were less than 9 mm and up to 21° for the comparison of *Geometry-Based 4D-CT* and *Grid-Based 4D-CT* (Table 3). The smallest differences were observed for ML translation (mean RMSE 3.3 mm) and SI translation (mean RMSE 5.5 mm). Average correlations were very high for all translations and flexion, moderate for tilt, and moderate negative for spin.

Table 3: Average root mean square errors (RMSEs) and Spearman correlation coefficients (r) for comparing Geometry-Based 4D-CT and Grid-Based 4D-CT, for all TF flexion angles and for the TF flexion angles in which the patella is engaged (TF flexion > 20°). Individual RMSE and r values can be found in Appendix E.

	RMSE (°/mm)		**Correlation (-)**	
	All	**Engaged**	**All**	**Engaged**
Spin (°)	26.5	20.4	-0.57	-0.54
Tilt (°)	17.2	18.1	0.09	0.49
Flexion (°)	13.6	6.9	0.65	1
AP translation (mm)	9.1	8.6	0.98	1
SI translation (mm)	9.6	5.5	0.94	1
ML translation (mm)	3.3	3.3	0.94	0.96

Most data fell within the limits of agreement of the Bland-Altman plot for the comparison of *Geometry-Based 4D-CT* and *Grid-Based 4D-CT*, both for all TF flexion angles (Figure 12) and for the TF flexion angles in which the patella is engaged (Figure 13). The data falling outside of the limits of agreement, mostly belonged to participant 2. For spin and tilt, there was a clear distinction between participant 2 and the other participants. For spin, flexion/extension, and ML translation, the points were approximately on a straight sloped line per participant, indicating that the difference between the two methods changes over the range of the measured rotations and translations.

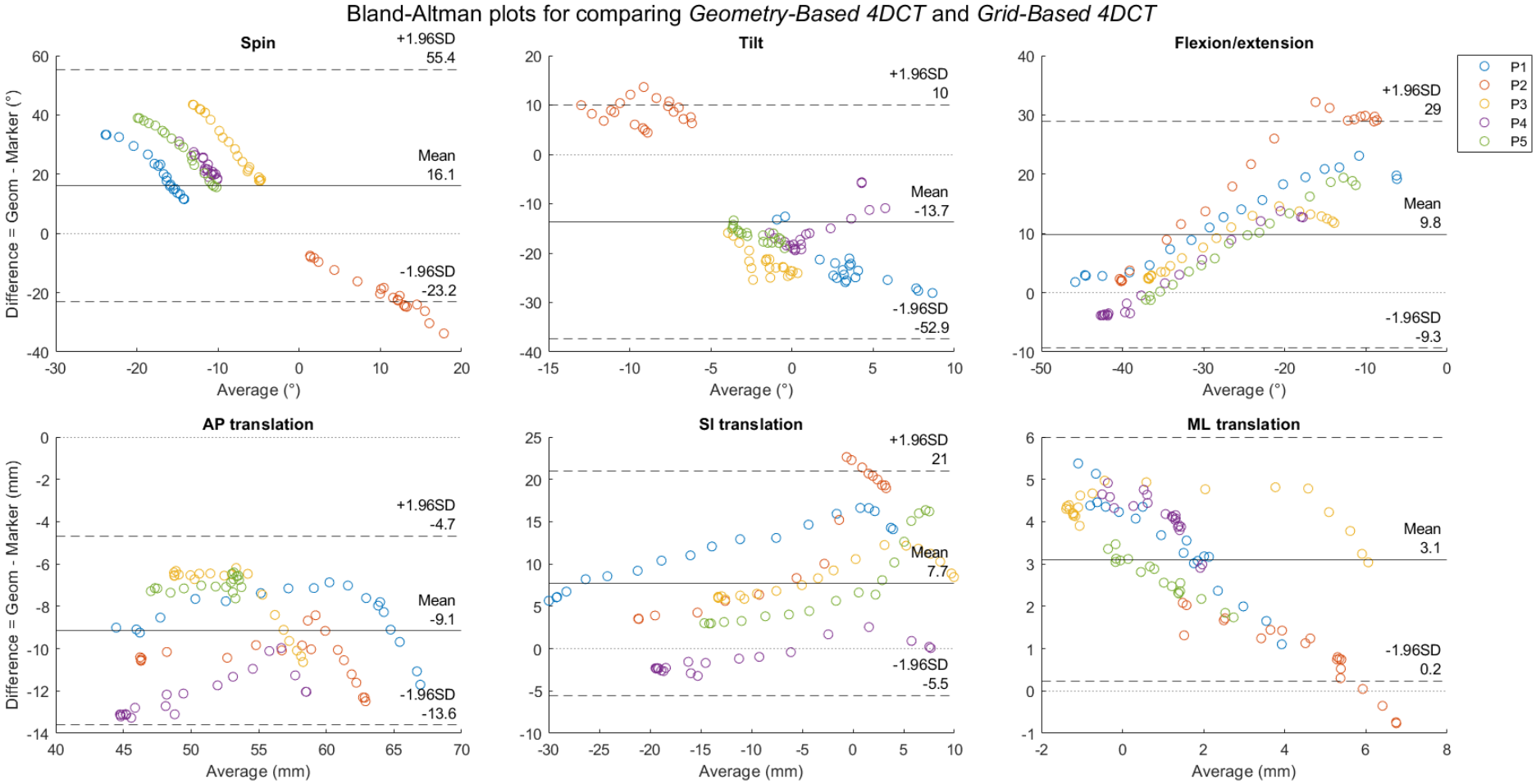

Figure 12: Bland-Altman plots for comparing Geometry-Based 4D-CT and Grid-Based 4D-CT, for all knee angles. Mean and difference were computed for each TF angle for which grid markers could be segmented, causing a different amount of data points per participant. Each colour represents a different participant.

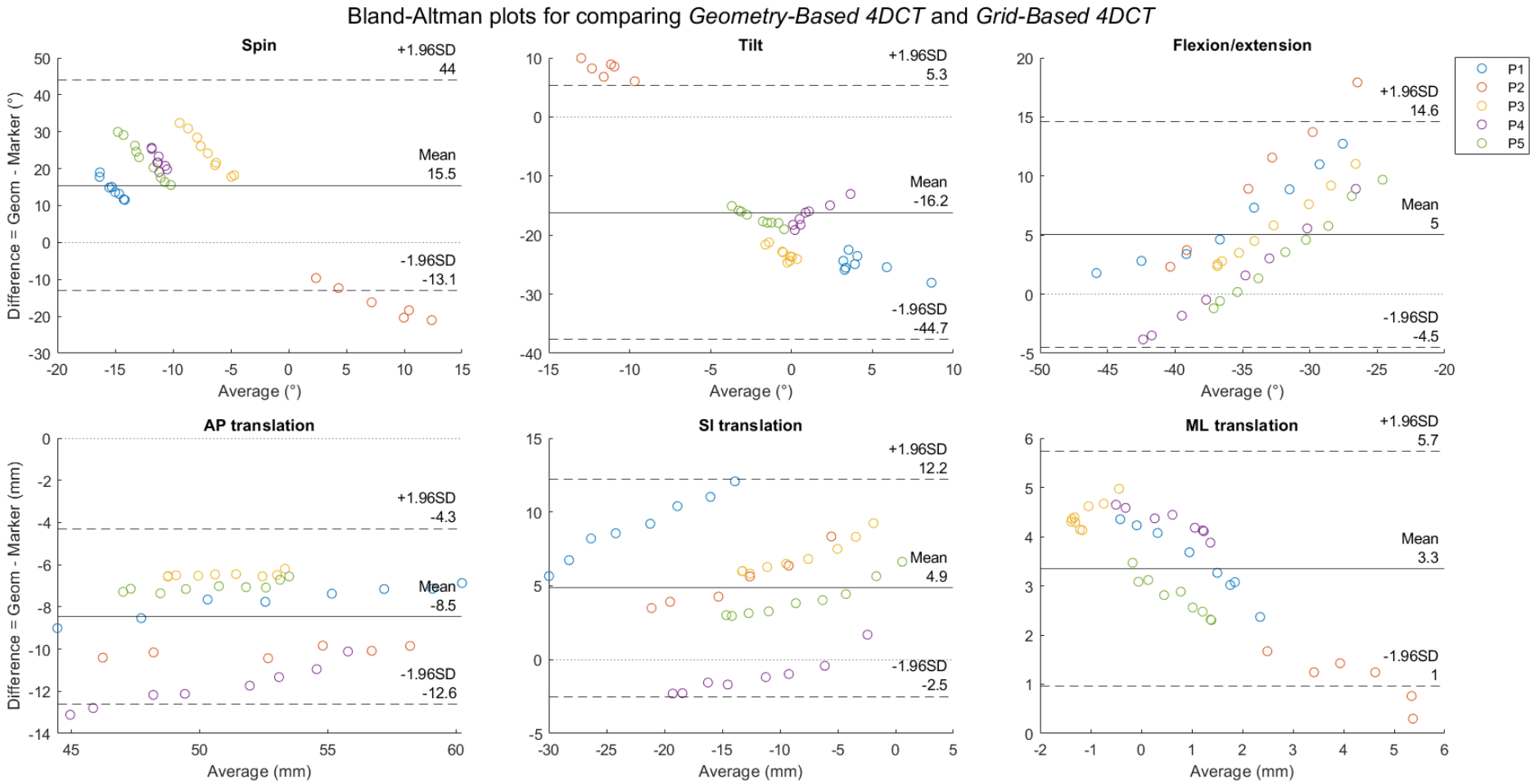

Figure 13: Bland-Altman plots for comparing Geometry-Based 4D-CT and Grid-Based 4D-CT, for the knee angles in which the patella is engaged (TF flexion > 20°). Mean and difference were computed for each TF angle for which grid markers could be segmented, causing a different amount of data points per participant.Each colour represents a different participant.

The final cost the ICP algorithm (see *Shape-Fitting Algorithm*) decreased with increasing TF flexion angle (Figure 14). Furthermore, the cost was substantially higher for participant 2 than for the other participants, indicating possible less reliable results for participant 2. Because of this and the large difference between participant 2 and the other four participant, all analyses were also performed excluding participant 2. These results can be found Appendix F.

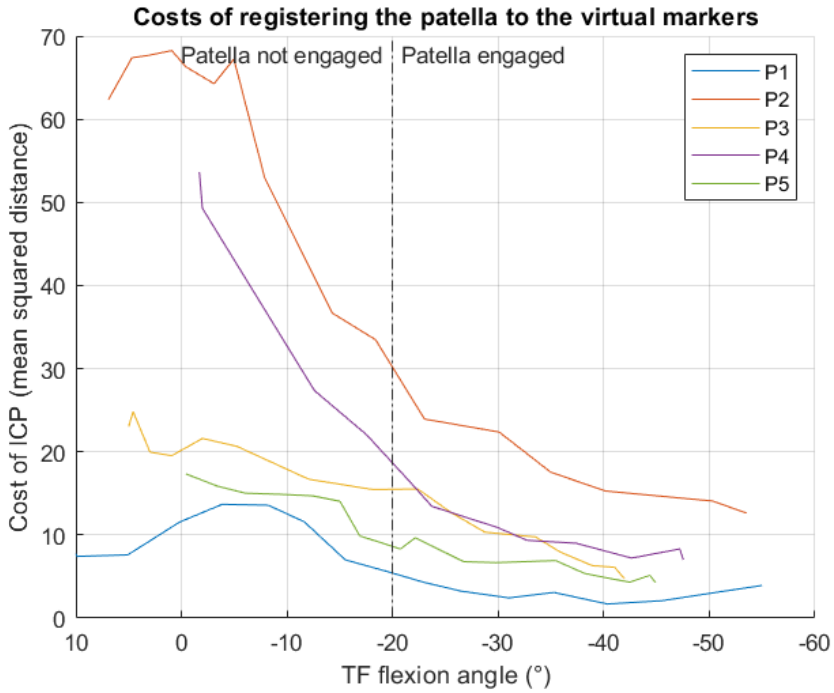

Figure 14: Cost in the last step of the ICP algorithm for each TF flexion angle. The cost is computed as the mean squared distance of the points on the patella mesh to the selected virtual grid markers. The cost is plotted against the TF flexion angle, which is computed using the tibial and femoral geometry. Each colour represents a different participant.

3.3 Grid-Based 4D-CT vs. Grid-Based OMC

Large differences between participant 2 and the other three participants were visible for both *Grid-Based OMC* and *Grid-Based 4D-CT* in for spin and tilt (Figure 15). Furthermore, large jumps were visible in the spin and tilt of participant 2.

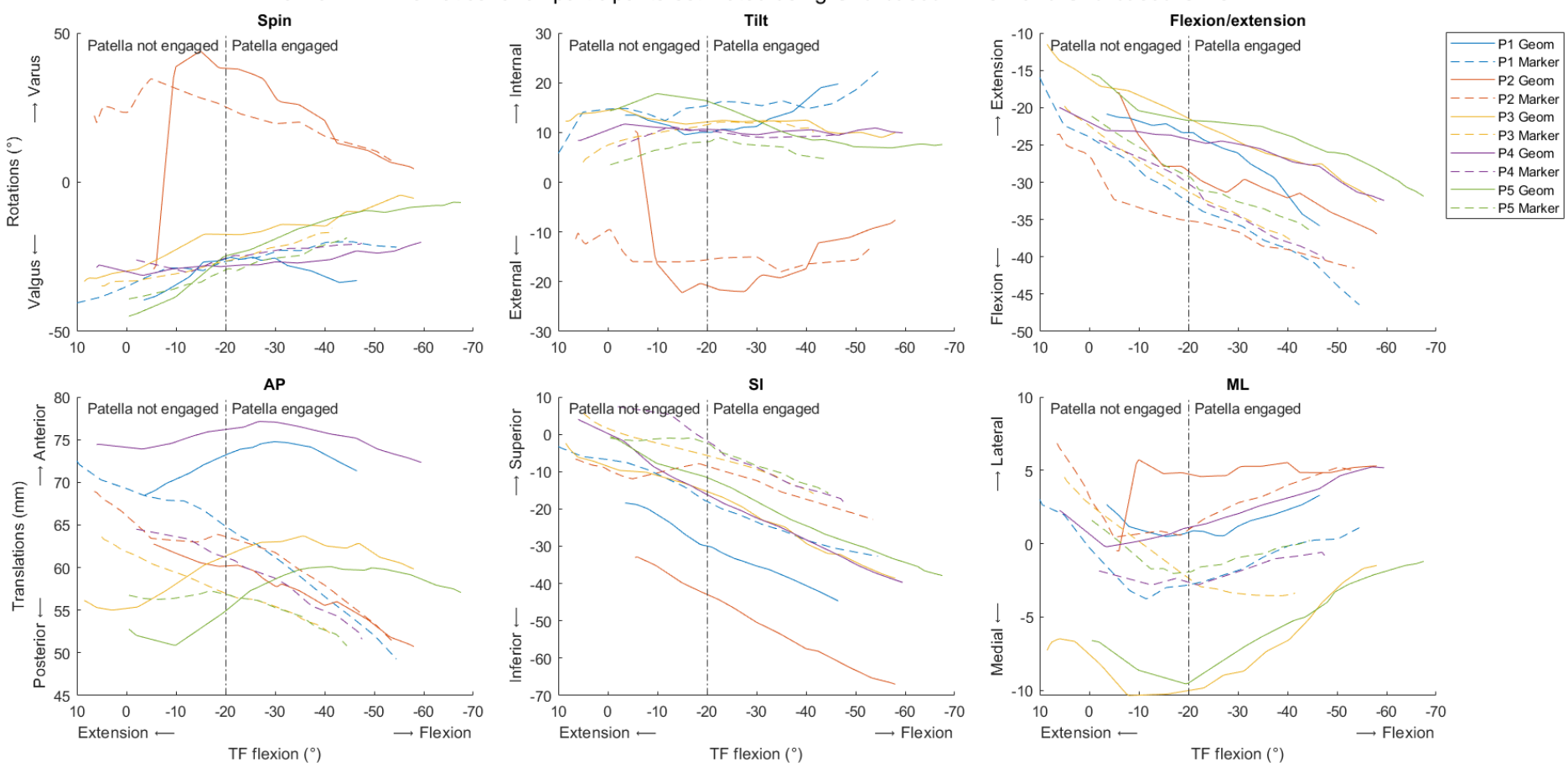

Figure 15: PF kinematics of all participants for Grid-Based OMC vs. Grid-Based 4D-CT. TF flexion angle is computed from tibial and femoral geometry for Grid-based 4D-CT and from tibia and femur markers for Grid-based OMC. Each colour represents a different participant.

Average RMSEs of the differences between the methods were up to 17 mm and 9° for the comparison of *Grid-Based OMC* and *Grid-Based 4D-CT* (Table 4). The smallest differences were observed for ML translation (mean RMSE 4.7 mm) and tilt (mean RMSE 4.3°). Correlations were very high for SI translation and flexion, high for spin, moderate for ML translation, and low or low negative for tilt and AP translation.

For the knee angles in which the patella is engaged, the average RMSEs of the differences between the methods were up to 18 mm and 11° for the comparison of *Grid-Based OMC* and *Grid-Based 4D-CT* (Table 4). The smallest differences were observed for ML translation (mean RMSE 3.8 mm) and tilt, (mean RMSE 3.2°). Correlations were high for SI translation and flexion, moderate for spin, AP translation, and ML translation, and low for tilt.

Table 4: Average root mean square errors (RMSEs) and Spearman correlation coefficients (r) for comparing Grid-Based OMC and Grid-Based 4D-CT, for all TF flexion angles and for the TF flexion angles in which the patella is engaged (TF flexion > 20°). Individual RMSE and r values can be found in Appendix E.

	RMSE (°/mm)		**Correlation (-)**	
	All	**Engaged**	**All**	**Engaged**
Spin (°)	5.9	5.9	0.81	0.56
Tilt (°)	4.3	3.2	0.14	0.32
Flexion (°)	8.5	9.3	0.98	0.94
AP translation (mm)	9.4	10.6	-0.13	0.39
SI translation (mm)	17.1	18.0	0.96	0.97
ML translation (mm)	4.7	3.8	0.53	0.53

Most data fell within the limits of agreement of the Bland-Altman plot for the comparison of *Grid-Based OMC* and *Grid-Based 4D-CT*, both for all TF flexion angles (Figure 16) and for the TF flexion angles in which the patella is engaged (Figure 17). Yet, there were quite some data points for tilt in all TF angles falling outside of the limits of agreement. Furthermore, there was a clear distinction between participant 2 and the other participants for flexion, tilt, and SI translation. Similarly, there was a distinction between participants 3 and 5, and participants 1, 2, and 4 for ML translation, and between participants 1 and 4, and participants 2, 3, and 5 for AP translation. Data did not seem to be on a straight sloped line.

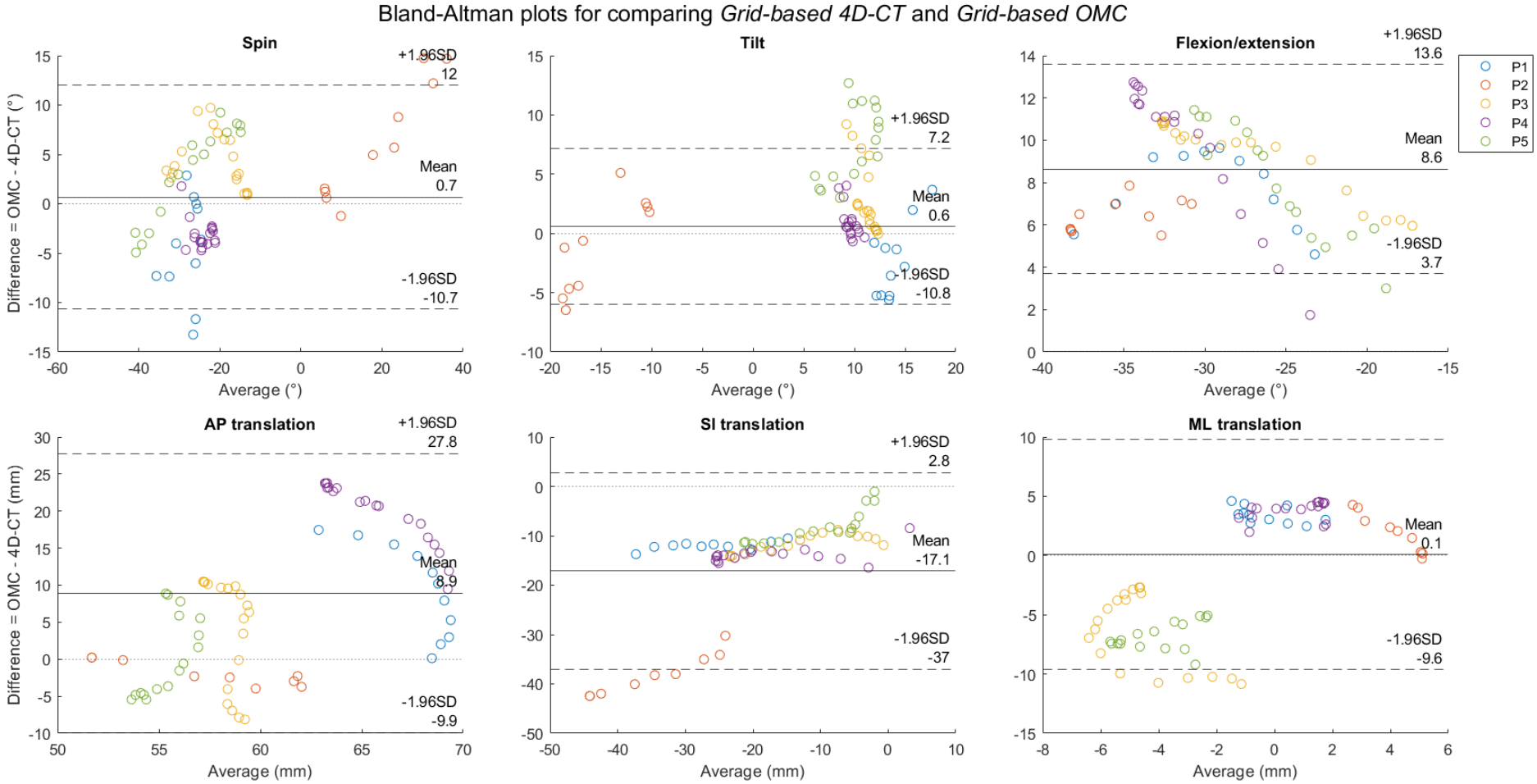

Figure 16: Bland-Altman plots for comparing Grid-Based OMC and Grid-Based 4D-CT, for all knee angles. Mean and difference were computed for each TF angle for which grid markers could be segmented in 4D-CT, causing a different amount of data points per participant. Each colour represents a different participant.

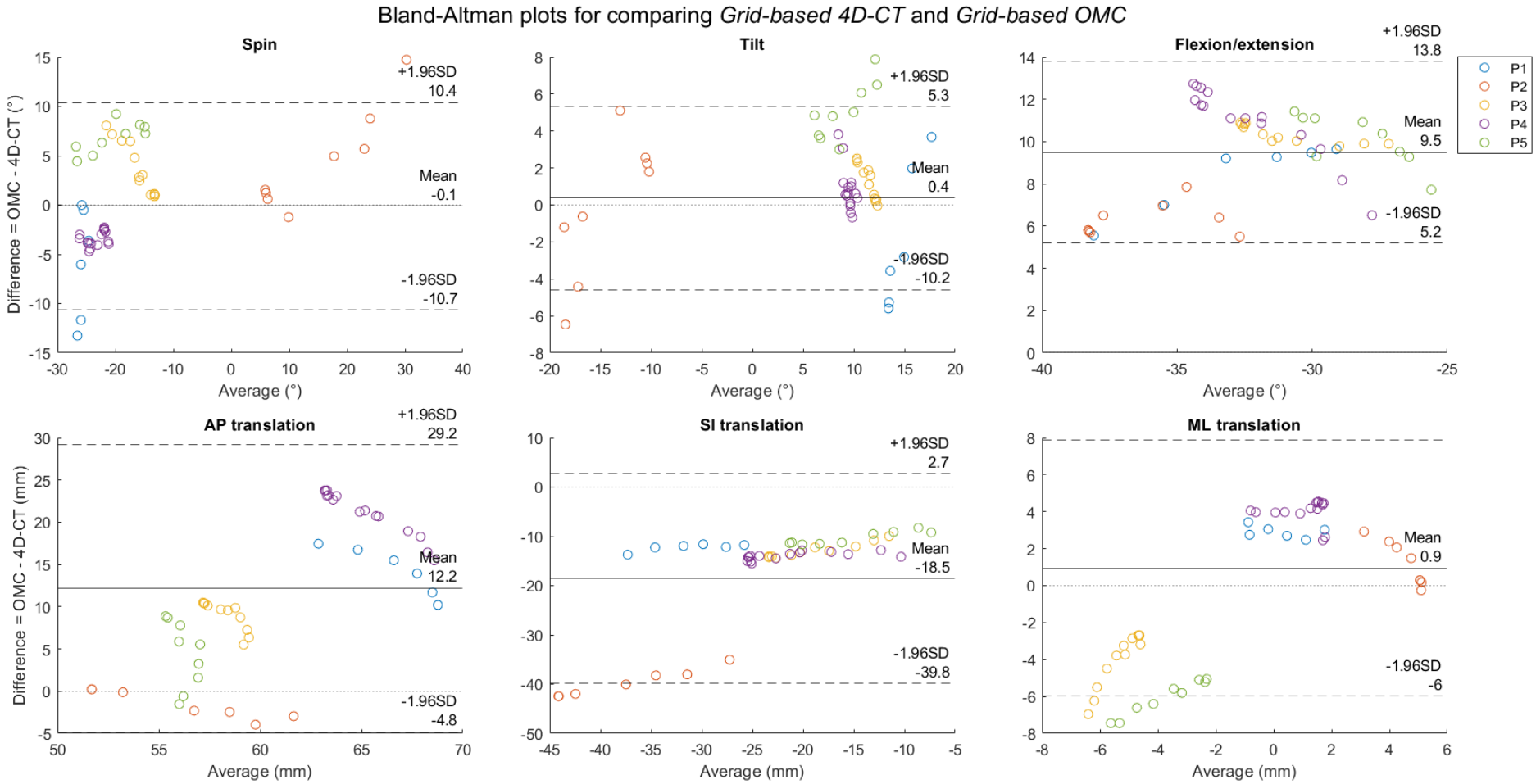

Figure 17: Bland-Altman plots for comparing Grid-Based OMC and Grid-Based 4D-CT, for the knee angles in which the patella is engaged (TF flexion > 20°). Mean and difference were computed for each TF angle for which grid markers could be segmented in 4D-CT, causing a different amount of data points per participant. Each colour represents a different participant.

PF angle was plotted against TF flexion angle, while the tibial and femoral ACSs were computed differently for the two methods. Despite the different ACSs, the TF flexion angles showed similar patterns for both methods (Figure 18). One difference between the methods was the range of the TF flexion angle, being larger for OMC for all participants but participant 1.

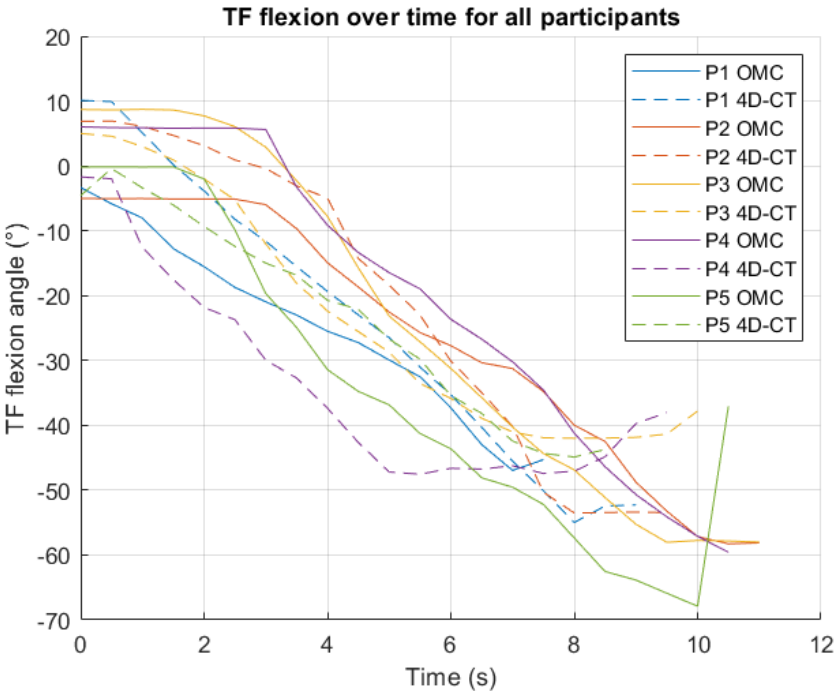

Figure 18: TF flexion angle for all participants computed using the two different methods. The angle was computed from tibial and femoral geometries for Grid-Based 4D-CT and from the tibia and femur markers for Grid-Based OMC. Each colour represents a different participant.

The final cost in the ICP algorithm for OMC decreased with increasing TF flexion angle (Figure 19). Furthermore, the cost was again substantially higher for participant 2 than for the other participants, indicating possible less reliable results for participant 2. Because of this and the large difference between participant 2 and the other four participant, all analyses were also performed excluding participant 2. These results can be found Appendix F.

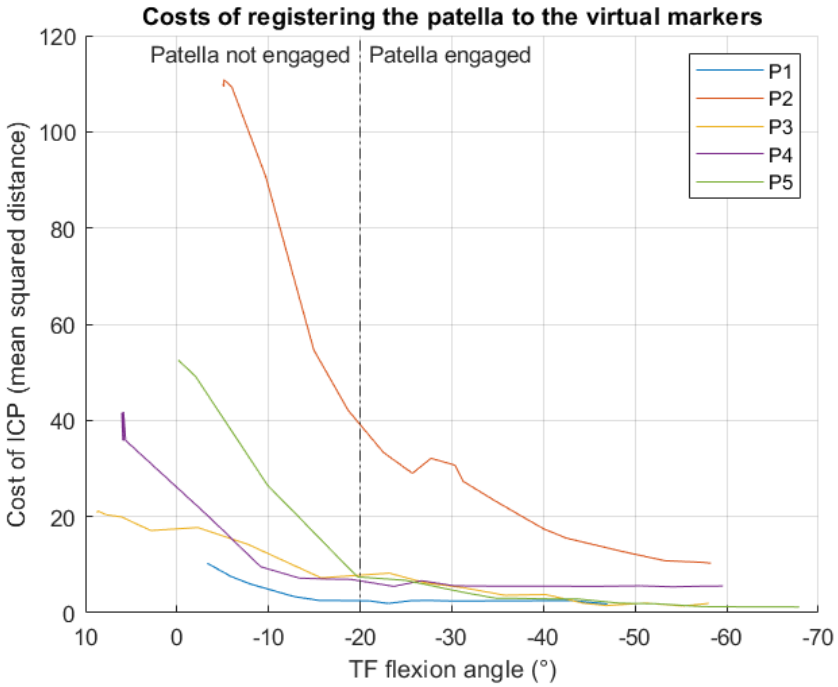

Figure 19: Cost in the last step of the ICP algorithm for OMC for each TF flexion angle. The cost is computed as the mean squared distance of the points on the patella mesh to the selected virtual grid markers. The cost is plotted against the TF flexion angle, which is computed using the tibia and femur markers in OMC. Each colour represents a different participant.

3.4 Influence of soft tissue artefacts and the definition of the femur ACS

The marker-based femur ACS rotated and translated differently than the geometry-based femur ACS for all participants (Figure 20). This resulted in a marker-based femur ACS that was gradually more flexed than the geometry-based femur ACS for increasing TF flexion (Figure 21). Furthermore, the marker-based femur ACS moved anteriorly, inferiorly, and medially with respect to the geometry-based femur ACS with increasing TF flexion.

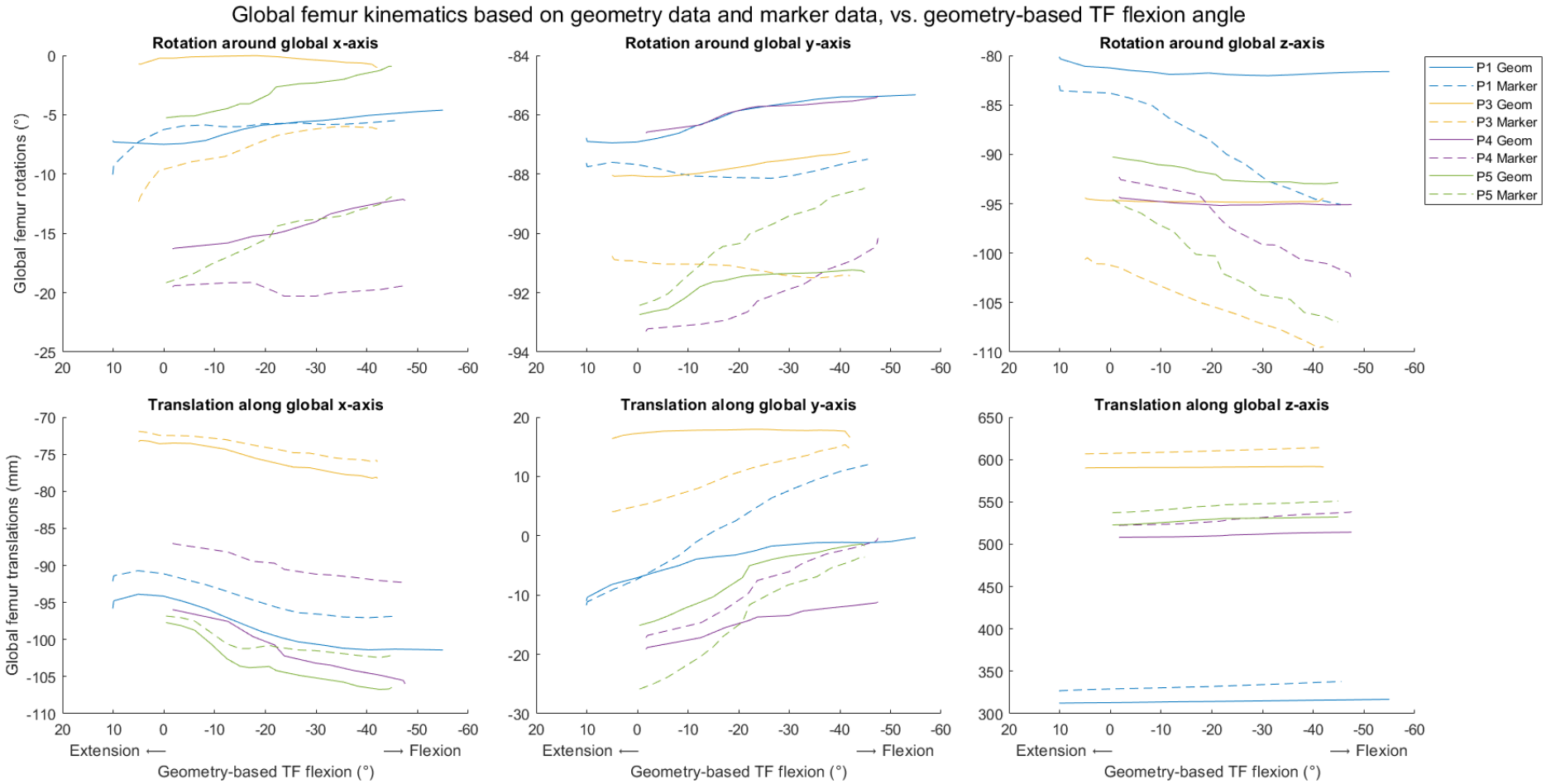

Figure 20: Global femur kinematics computed from bone geometries, and from marker locations, both measured using 4D-CT. Each colour represents a different participant.

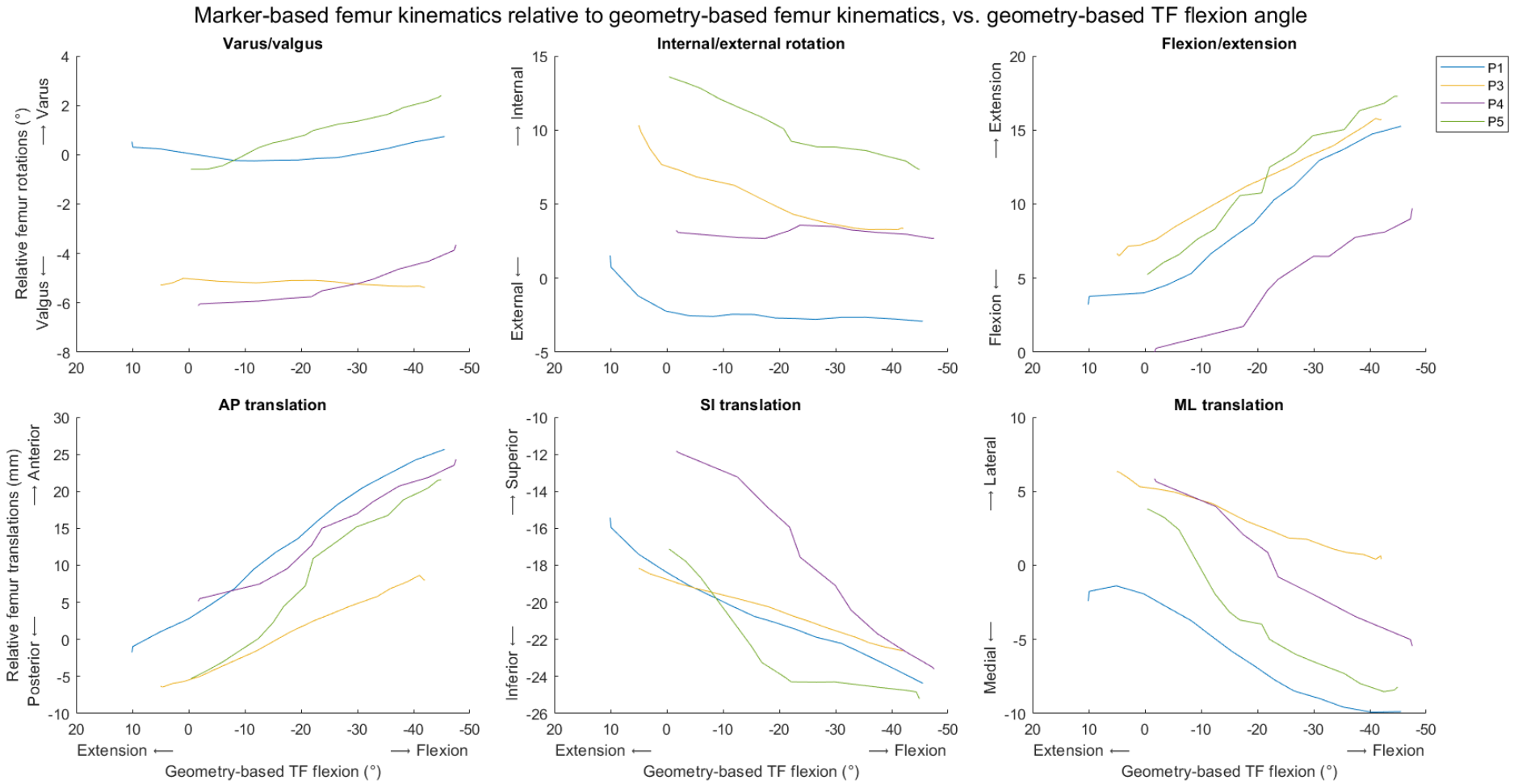

Figure 21: Relative kinematics of the femur ACS computed from marker locations relative to the femur ACS computed from bone geometries, both measured using 4D-CT. Each colour represents a different participant.

4 Discussion

We developed a new method to measure 6 DoF patellofemoral kinematics using optical motion capture with a knee marker grid, and a shape fitting algorithm. The results showed that, when measured using 4D-CT, PF flexion and all PF translations could be estimated from the marker grid using a shape fitting algorithm. However, measuring the marker grid using OMC led to large errors in the PF kinematics.

4.1 Geometry-Based 4D-CT vs. Grid-Based 4D-CT

To validate the use of a shape fitting algorithm in our method, we compared PF kinematics obtained from bone movements measured using 4D-CT with PF kinematics obtained by applying the shape fitting algorithm on the locations of the grid markers measured using 4D-CT.

The final cost of the ICP in the shape fitting algorithm decreased for increasing knee flexion, indicating that the fit between the patella shape and the virtual markers is better for higher knee flexion. This supports the assumption that the patella protrudes less through the skin for extended knees than for flexed knees, and indicates that the results based on the TF flexion angles in which the patella is engaged (TF > 20°) might be more reliable than the results based on all TF flexion angles. In general, RMSEs were smaller and correlations higher for the engaged TF flexion angels than for the full range of TF angles, indicating that the method indeed performs better for the engaged TF flexion angles.

4.1.1 PF Rotations

The average RMSE for flexion in the engaged TF flexion angles was 6.9°, which is less than the error found by Inai et al. (2020). The very high correlation and the distribution of the data points in the Bland-Altman plots indicate that the estimated PF flexion shows a similar pattern for both methods, but that the difference between the methods linearly changes for increasing TF flexion. For spin and tilt, RMSEs were over 17° and correlations were poor, even when only including the engaged TF flexion angles.

It is remarkable that the tilt and spin angles estimated using the shape fitting for participant 2 were highly different from the spin and tilt angles estimated for the other four participants, being almost mirrored around zero (Figure 11). Since the final costs of the ICP algorithm for participant 2 were higher than the costs for the other participants, it might indicate that the ICP algorithm could not find a good fit between the patella and the virtual markers. A possible cause could be that the patella of participant 2 did not protrude enough through the skin to be visible in the locations of the virtual markers, for example due to more soft tissue around the skin.

4.1.2 PF Translations

For the PF translations, average RMSEs ranged from 3.3 mm to 9.1 mm when including all TF flexion angles, and from 3.3 mm to 8.6 mm when including only the engaged TF flexion angles. These errors were smaller than the errors reported by Inai et al. (2020), but larger than the errors reported by Zandee (2022). All correlations for PF translations were very high, indicating that the errors were caused by a systematic difference between the two methods.

For AP translation, a systematic difference was expected since the patella mesh is fitted onto the centre locations of the knee grid markers on top of the skin. This causes the anterior side of the patella mesh to be estimated to be in front of the skin overlying the knee. The skin overlying the patella is around 7 mm thick (Hu et al., 2024) and the grid markers have a radius of 2 mm. The total expected systematic difference thus is around 9 mm, which is around the same size as the average RMSE for AP translation (8.6 – 9.1 mm). When subtracting the expected systematic difference, the RMSE would be similar to the size of the errors reported by Zandee (2022).

An explanation for the errors of SI and ML translation being larger than those reported by Zandee (2022) could be that he normalised the data by setting all PF translations to 0 mm at maximum knee flexion to compensate for offsets caused by the different methods. Since there appeared to be a systematic error between the two methods in our data, such a normalisation would likely have decreased our errors too. However, we decided not to do a normalisation, since it discards information on the difference between methods (such as the presence and direction of systematic errors).

4.1.3 Implications

Overall, tilt and spin could not be estimated using a knee marker grid and a shape fitting algorithm. For PF flexion and all PF translations, the errors were smaller than the errors reported by Inai et al. (2020), but larger than the errors reported by Zandee (2022). The DoF that are clinically most relevant for patellofemoral pain are spin, tilt, and ML translation (Draper et al., 2011; MacIntyre et al., 2006). Of those, two could unfortunately not be estimated using this method.

The errors reported for the PF rotations and translations were larger than those reported for methods that directly measured PF kinematics in functional weight-bearing activities. However, the errors were similar to the errors reported for most mathematical models estimating the PF kinematics (Peeters et al., 2024).

4.2 Grid-Based 4D-CT vs. Grid-Based OMC

As further validation, we compared the PF kinematics obtained by applying the shape fitting algorithm on the grid marker locations measured using either 4D-CT or OMC. This comparison was meant to indicate whether our shape fitting algorithm could also be used with OMC.

The final cost of the ICP in the shape fitting algorithm for the OMC data again decreased for increasing knee flexion, indicating that the results based on the TF flexion angles in which the patella is engaged (TF > 20°) might be more reliable than the results based on all TF flexion angles. However, RMSEs were not necessarily smaller and correlations not necessarily higher for the engaged TF flexion angels than for the full range of TF flexion angles, indicating that the performance of the method did not depend on the patella being engaged or not. Furthermore, there was again a large difference in the costs for participant 2 and the other four participants.

4.2.1 PF rotations

Average RMSEs for all rotations ranged from 4.3 to 8.5° including all TF flexion angles, and from 3.2 to 9.3° including only the engaged TF flexion angles. These errors are all lower than the errors reported

by Inai et al. (2020). Correlations were moderate for spin and very high for flexion, both including all and only the engaged TF flexion angles, but low for tilt.

There was a remarkable large jump in the tilt and spin data for participant 2 in the region of the TF flexion angles where the patella is not engaged. This was probably caused by the patella not protruding through the skin enough for the ICP algorithm to find a good fit. Yet, excluding participant 2 (because of the high final cost), did not improve the results (Appendix F).

4.2.2 PF translations

Average RMSEs ranged from 4.7 mm for ML translation to 17.1 mm for SI translation in all TF flexion angles, and from 3.8 mm for ML translation to 18.0 mm for SI translation in the engaged TF flexion angles. These errors are larger than the errors reported by Zandee (2022) and Inai et al. (2020). Furthermore, the correlations were very high for SI translation, moderate for ML translation, and low negative or moderate for AP translation (for all TF flexion angles or the engaged TF flexion angles). The large RMSE for SI translation was mainly caused by participant 2 (RMSE of around 40 mm). When excluding this participant, the RMSEs for SI translation decreased to 11.7 mm for all TF flexion angles and 12.4 mm for the engaged TF flexion angles, both still higher than the errors reported by Inai et al. (2020).

4.2.3 Implications

Overall, the difference between measuring the marker grid with OMC or 4D-CT was large for SI translation and the correlations were low for AP translation and ML translation. Since the shape fitting algorithm seemed unreliable for spin and tilt when comparing *Geometry-based 4D-CT* and *Grid-Based 4D-CT*, this indicates that the proposed method is only suitable to measure PF flexion.

However, the differences between *Grid-based 4D-CT* and *Grid-based OMC* are mainly caused by the way the grid markers are measured and are thus not influenced by the shape fitting algorithm. It could be that the accuracy of the OMC system was lower than the accuracy of the of the 4D-CT system. The cameras in the OMC system are normally attached to rails at about two meters above the ground. However, since the participants lay on their belly, three cameras were removed from the rails and placed on the ground to be able to see the knee grid markers (Figure 2). This imposed a high risk of slight changes in the positioning of the cameras during the measurement, which highly influences the accuracy if the system is not re-calibrated. Furthermore, by placing only three cameras on the ground, most markers could be seen by a maximum of two cameras. Although being seen by two cameras is sufficient to reconstruct the 3D marker location, the accuracy of the reconstruction improves with more cameras (Begon & Lacouture, 2010). Part of the difference between *Grid-based 4D-CT* and *Grid-based OMC* might thus be explained by the accuracy and setup of the OMC system.

4.3 Influence of soft tissue artefacts and the definition of the femur ACS

The difference in movement of the marker-based femur ACS and the geometry-based femur ACS was substantial. The geometry-based femur ACS was relatively stationary, as would be expected for the prone EF movement. The movement of the marker-based femur ACS indicates that soft tissue artefacts (STAs) and the definition of the femur ACS introduced errors in the computation of the

femur ACS. A possible source of error could be the placement of the third femur marker (the FEXTRA marker). This marker was not placed on a landmark for which the STA is expected to be minimum, but on a location within the scanning window of the CT-scanner, likely introducing STAs. Furthermore, the SI-axis of the marker-based femur ACS was defined as the line through the LEC and FEXTRA marker. This might not coincide with the SI-axis of the geometry-based femur ACS, which was defined as the third inertial axis of the femur. It likely also does not coincide with the ISB convention, which defines the SI-axis as the line through the centre of the epicondyles and the hip joint centre (Robinson & Vanrenterghem, 2012).

Since PF kinematics are computed as the movement of the patella with respect to the femur, errors in the estimation of the femur movement can have a large influence on the estimated PF kinematics. However, within each comparison, the same femur ACS was used to compute the PF kinematics (Table 2). The difference could only have influenced the TF flexion angle in the comparison of *Grid-based 4D-CT* vs. *Grid-based OMC*, but the TF flexion angle was similar for both methods (Figure 18). Yet, the influence of STAs and the definition of the femur ACS is something that should be considered when measuring PF kinematics using OMC.

4.4 Limitations and recommendations

A limitation of the present study is that the 4D-CT and OMC measurements took place at different moments. This introduces two sources of error in the comparison of *Grid-based 4D-CT vs. Grid-based OMC*. First, participants are probably not performing a movement exactly the same when doing it twice. To mitigate this issue, PF kinematics were plotted versus TF flexion angles. Second, the knee markers had to be removed between the two measurement sessions. Although the marker locations were drawn on the skin, the marker locations will never be exactly the same when applying them twice. This makes it more difficult to compare the 4D-CT and OMC data. However, the locations of the grid markers are not used directly but are interpolated. Therefore, a small deviation in the marker placement would probably not make a large difference. This is not the case for the femur markers, since their location is directly used to compute the femur ACS. A small deviation in the placement of the femur markers could thus directly influence the estimated PF kinematics. To overcome this limitation future research should perform the OMC and validation measurements simultaneously, for example using biplane-fluoroscopy.

Furthermore, performing the EF movement while lying prone imposes an extra difficulty in the shape fitting algorithm. When lying prone, gravity pulls skin and soft tissues towards the patella. This causes the patella to be less prominent compared to for example lying supine. During functional weight-bearing tasks, gravity pulls the skin and soft tissues towards the inferior direction of the patella. This of course causes differences compared to lying prone. Future research should take the influence of the gravity on the performance of the shape fitting algorithm into consideration when deciding on the movement task.

Moreover, this method is highly dependent on the patella being prominently visible on the skin. Therefore, it might not be usable for people with thick soft tissue overlying the patella. The average BMI of our participants was 22 kg/m^2, indicating a healthy weight (WHO, 2010), but this does not necessarily indicate a low soft tissue thickness over the patella. Future research should investigate the performance of the method in participants with different BMIs and different soft tissue thicknesses.

Another limitation is that the performed EF movement is not a functional weight-bearing task, although the aim was to develop a method able to measure PF kinematics during functional weight-bearing tasks. However, the aim of this particular study was to validate the method with 4D-CT and functional weight-bearing tasks are not possible within a CT scanner. When using e.g. fluoroscopy, it would be possible to validate the method during functional weight-bearing tasks such as squatting.

Furthermore, the use of the participant-specific patella as patella shape, makes the method dependent on the availability of radiation-requiring CT-scanning. To avoid this, an average patella shape could be used, such as a Statistical Shape Model (Eijkenboom et al., 2021). Before applying such a Statistical Shape Model to the shape fitting algorithm, the mode of variation most accurately reflecting the shape of the participants patella should then be identified from the skin deformation, for example by measuring the width and height, or the circumference of the protruded patella.

Finally, the accuracy of the results might have been influenced by the limited number of grid markers available. To cover the skin area overlaying the patellar range of motion, grid markers had to be placed at horizontal and vertical distances of around 17.5 and 20 mm. No measured information on the deformation of the skin was available between the grid markers. When the edge of the patella falls between the grid markers, the shape might thus be less visible in the locations of the grid markers. Smaller distances between the grid markers might overcome this issue. Yet, no clear differences were observed for participants 1 and 2 (distance of 20 mm) and participants 3, 4, and 5 (distance of 17.5 mm). On the other hand, Inai et al. (2020) found that an inter-marker distance of 10 mm led to better results than inter-marker distances of 15 and 20 mm. However, when using the grid markers with OMC, decreasing the distance between the grid markers might lead to difficulties distinguishing the grid markers. Therefore, future research should aim to find the optimum distance between the grid markers minimizing the issue of missing deformation information between the grid markers, without imposing problems with distinguishing the markers in OMC.

To improve the shape fitting algorithm, deep learning could be used to estimate the location and orientation of the patella shape from the knee marker grid. Deep learning has been used before to estimate kinematics of a knee prosthesis from fluoroscopy images (Nguyen, 2023). A deep learning model for estimating the PF kinematics could be trained on the Grid-based 4D-CT data, using the Geometry-based 4D-CT data as ground truth. However, large data sets would be required to effectively train the deep learning model.

4.5 Conclusion

We developed a new method to measure 6 DoF patellofemoral kinematics using optical motion capture with a knee marker grid, and a shape fitting algorithm. The shape fitting algorithm was able to estimate PF flexion and all three PF translations when the marker grid was measured using 4D-CT. However, it was not able to estimate PF spin and tilt, which are clinically relevant kinematics. Furthermore, measuring the marker grid using OMC led to large errors compared to 4D-CT, which were probably introduced by the accuracy of the measurement system or by the definitions of the ACSs. Overall, the shape fitting algorithm thus seems to be able to estimate PF flexion and all three PF translations from a marker grid, but applying it to OMC data is not valid yet.

References

Akbarshahi, M., Schache, A. G., Fernandez, J. W., Baker, R., Banks, S., & Pandy, M. G. (2010). Non-invasive assessment of soft-tissue artifact and its effect on knee joint kinematics during functional activity. *Journal of Biomechanics*, *43*(7), 1292–1301. https://doi.org/10.1016/j.jbiomech.2010.01.002

Begon, M., & Lacouture, P. (2010). Accuracy of 3-D Reconstruction with Occlusions. *Journal of Applied Biomechanics*, *26*(1), 104–108. https://doi.org/10.1123/jab.26.1.104

Besl, P. J., & McKay, N. D. (1992). A method for registration of 3-D shapes. *IEEE Transactions on Pattern Analysis and Machine Intelligence*, *14*(2), 239–256. https://doi.org/10.1109/34.121791

Charbonnier, C., Chagué, S., Kolo, F. C., Chow, J. C. K., & Lädermann, A. (2014). A patient-specific measurement technique to model shoulder joint kinematics. *Orthopaedics & Traumatology: Surgery & Research*, *100*(7), 715–719. https://doi.org/10.1016/j.otsr.2014.06.015

Chen, H., Kluijtmans, L., Bakker, M., Dunning, H., Kang, Y., van de Groes, S., Sprengers, A. M. J., & Verdonschot, N. (2020). A robust and semi-automatic quantitative measurement of patellofemoral instability based on four dimensional computed tomography. *Medical Engineering & Physics*, *78*, 29–38. https://doi.org/10.1016/j.medengphy.2020.01.012

Coburn, S. L., Barton, C. J., Filbay, S. R., Hart, H. F., Rathleff, M. S., & Crossley, K. M. (2018). Quality of life in individuals with patellofemoral pain: A systematic review including meta-analysis. *Physical Therapy in Sport*, *33*, 96–108. https://doi.org/10.1016/j.ptsp.2018.06.006

Colvin, A. C., & West, R. V. (2008). Patellar Instability. *The Journal of Bone and Joint Surgery-American Volume*, *90*(12), 2751–2762. https://doi.org/10.2106/JBJS.H.00211

Crossley, K. M., Stefanik, J. J., Selfe, J., Collins, N. J., Davis, I. S., Powers, C. M., McConnell, J., Vicenzino, B., Bazett-Jones, D. M., Esculier, J.-F., Morrissey, D., & Callaghan, M. J. (2016). 2016 Patellofemoral pain consensus statement from the 4th International Patellofemoral Pain Research Retreat, Manchester. Part 1: Terminology, definitions, clinical examination, natural history, patellofemoral osteoarthritis and patient-reported outcome measures. *British Journal of Sports Medicine*, *50*(14), 839–843. https://doi.org/10.1136/bjsports-2016-096384

Dawson-Haggerty, M. (2023). `trimesh` (Version 4.1.8). Retrieved from https://trimsh.org

Draper, C. E., Besier, T. F., Fredericson, M., Santos, J. M., Beaupre, G. S., Delp, S. L., & Gold, G. E. (2011). Differences in patellofemoral kinematics between weight-bearing and non-weight-bearing conditions in patients with patellofemoral pain. *Journal of Orthopaedic Research*, *29*(3), 312–317. https://doi.org/10.1002/jor.21253

Eijkenboom, J. J., Tümer, N., Waarsing, E. H., van der Heijden, R. A., Cheng, R., Sheehan, F. T., Oei, E. H., Zadpoor, A. A., Bierma-Zeinstra, S. M., & van Middelkoop, M. (2021). Patellofemoral pain patients show differences in 3D patellar shape compared to healthy control subjects. *Osteoarthritis and Cartilage*, *29*, S336–S337. https://doi.org/10.1016/j.joca.2021.02.438

Fedorov, A., Beichel, R., Kalpathy-Cramer, J., Finet, J., Fillion-Robin, J.-C., Pujol, S., Bauer, C., Jennings, D., Fennessy, F., Sonka, M., Buatti, J., Aylward, S., Miller, J. V, Pieper, S., & Kikinis, R. (2012). 3D Slicer as an image computing platform for the Quantitative Imaging Network. *Magnetic Resonance Imaging*, *30*(9), 1323–1341. https://doi.org/10.1016/j.mri.2012.05.001

Fick, C. N., Jiménez-Silva, R., Sheehan, F. T., & Grant, C. (2022). Patellofemoral kinematics in patellofemoral pain syndrome: The influence of demographic factors. *Journal of Biomechanics*, *130*, 110819. https://doi.org/10.1016/j.jbiomech.2021.110819

Hu, H., Tao, Y., Qingyuan, Z., Zhang, quoqiang, & Ni, M. (2024). X-ray measurement of periarticular soft tissue predict readmission complications after Total Knee Arthroplasty. *MedRxiv*.

Inai, T., Takabayashi, T., Watanabe, S., Ikezu, M., Kaneko, F., Matsuzawa, K., & Edama, M. (2020). A new method for estimating three-dimensional movement of the patella using a surface mapping method and computed tomography. *Heliyon*, *6*(8), e04729. https://doi.org/10.1016/j.heliyon.2020.e04729

MacIntyre, N. J., Hill, N. A., Fellows, R. A., Ellis, R. E., & Wilson, D. R. (2006). Patellofemoral Joint Kinematics in Individuals with and without Patellofemoral Pain Syndrome. *The Journal of Bone & Joint Surgery*, *88*(12), 2596–2605. https://doi.org/10.2106/JBJS.E.00674

Macri, E. M. (1997). *PATELLOFEMORAL OSTEOARTHRITIS: CHARACTERIZING KNEE ALIGNMENT AND MORPHOLOGY*.

MathWorks. (2022). MATLAB R2021a. Retrieved from https://www.mathworks.com/products/matlab.html

Mattson, J. M., Russo, S. A., Rose, W. C., Rowley, K. M., & Richards, J. G. (2012). Identification of scapular kinematics using surface mapping: A validation study. *Journal of Biomechanics*, *45*(12), 2176–2179. https://doi.org/10.1016/j.jbiomech.2012.05.048

Miranda, D. L., Rainbow, M. J., Crisco, J. J., & Fleming, B. C. (2013). Kinematic differences between optical motion capture and biplanar videoradiography during a jump–cut maneuver. *Journal of Biomechanics*, *46*(3), 567–573. https://doi.org/10.1016/j.jbiomech.2012.09.023

Nguyen, V. D. (2023). *An Automated, Deep Learning Approach to Systematically & Sequentially Derive Three-Dimensional Knee Kinematics Directly from Two-Dimensional Fluoroscopic Video* [PhD Dissertation]. University of Tennessee.

Oh, H., & Kim, J. (2017). *Patella Shape Extraction from 3D Point Cloud Data for Personalized Knee Brace* (pp. 160–168). https://doi.org/10.1007/978-3-319-58463-8_14

Oosterbaan, F. A. (2023). *4DCT as a tool to evaluate kinematic changes due to ACL injury: Determination of a workflow for the clinical setting* [Master's Thesis, Delft University of Technology]. http://resolver.tudelft.nl/uuid:aa93201d-6b1a-494f-a496-86fd23f17649

Peeters, L. M., Wesseling, M., Macri, E. M., Heyns, K., & Harlaar, J. (2024). *Methods used to noninvasively quantify patellofemoral kinematics during functional movements: A systematic review.* [Unpublished Manuscript]. Delft University of Technology.

Powers, C. M., Witvrouw, E., Davis, I. S., & Crossley, K. M. (2017). Evidence-based framework for a pathomechanical model of patellofemoral pain: 2017 patellofemoral pain consensus statement from the 4th International Patellofemoral Pain Research Retreat, Manchester, UK: part 3. *British Journal of Sports Medicine*, *51*(24), 1713–1723. https://doi.org/10.1136/bjsports-2017-098717

Qualisys. (2020). Qualisys Track Manager (Version 2023.2). Retrieved from https://www.qualisys.com/software/qualisys-track-manager/

Robinson, M. A., & Vanrenterghem, J. (2012). An evaluation of anatomical and functional knee axis definition in the context of side-cutting. *Journal of Biomechanics*, *45*(11), 1941–1946. https://doi.org/10.1016/j.jbiomech.2012.05.017

Smith, B. E., Selfe, J., Thacker, D., Hendrick, P., Bateman, M., Moffatt, F., Rathleff, M. S., Smith, T. O., & Logan, P. (2018). Incidence and prevalence of patellofemoral pain: A systematic review and meta-analysis. *PLOS ONE*, *13*(1), e0190892. https://doi.org/10.1371/journal.pone.0190892

Taylor, R. (1990). Interpretation of the Correlation Coefficient: A Basic Review. *Journal of Diagnostic Medical Sonography*, *6*(1), 35–39. https://doi.org/10.1177/875647939000600106

Thorstensson, C. A., Andersson, M. L. E., Jonsson, H., Saxne, T., & Petersson, I. F. (2009). Natural course of knee osteoarthritis in middle-aged subjects with knee pain: 12-year follow-up using clinical and radiographic criteria. *Annals of the Rheumatic Diseases*, *68*(12), 1890–1893. https://doi.org/10.1136/ard.2008.095158

Utting, M. R., Davies, G., & Newman, J. H. (2005). Is anterior knee pain a predisposing factor to patellofemoral osteoarthritis? *The Knee*, *12*(5), 362–365. https://doi.org/10.1016/j.knee.2004.12.006

Wheatley, M. G. A., Rainbow, M. J., & Clouthier, A. L. (2020). Patellofemoral Mechanics: a Review of Pathomechanics and Research Approaches. *Current Reviews in Musculoskeletal Medicine*, *13*(3), 326–337. https://doi.org/10.1007/s12178-020-09626-y

WHO. (2010). *A healthy lifestyle - WHO recommendations*. Https://Www.Who.Int/Europe/News-Room/Fact-Sheets/Item/a-Healthy-Lifestyle---Who-Recommendations.

Wong, M. T., Wiens, C., Kuczynski, M., Manske, S., & Schneider, P. S. (2022). Four-dimensional computed tomography: musculoskeletal applications. *Canadian Journal of Surgery*, *65*(3), E388–E393. https://doi.org/10.1503/cjs.023420

Wyndow, N., Collins, N., Vicenzino, B., Tucker, K., & Crossley, K. (2016). Is There a Biomechanical Link Between Patellofemoral Pain and Osteoarthritis? A Narrative Review. *Sports Medicine*, *46*(12), 1797–1808. https://doi.org/10.1007/s40279-016-0545-6

Yu, Z., Yao, J., Wang, X., Xin, X., Zhang, K., Cai, H., Fan, Y., & Yang, B. (2019). Research Methods and Progress of Patellofemoral Joint Kinematics: A Review. *Journal of Healthcare Engineering*, *2019*, 1–13. https://doi.org/10.1155/2019/9159267

Zandee, W. (2022). *Patellar tracking using a grid of skin mounted markers evaluated by four dimensional computed tomography* [Master's Thesis, Delft University of Technology]. http://resolver.tudelft.nl/uuid:cc1b04ee-8da2-4af0-9a62-74f3d4b52010

Appendices

Appendix A. Protocol OMC measurements

Our aim is to measure kinematics and kinetics during movement, in particular of the knee, for use in a multiscale modelling framework. This will be done by placing 49 small markers on the knee, to measure patella kinematics, and 28 normal markers on the legs and the torso as well as measuring ground reaction forces. For validation purposes, we will also measure EMG activity of a set of knee muscles.

1. Equipment

First finish this checklist to make sure everything that is needed is in the lab.

28 **normal** reflective markers (19 mm)	
49 **small** reflective markers (4 mm)	
4 clusters with reflective markers (19 mm)	
10 EMG sensors (DELSYS)	
5 force plates	
Double-sided tape	
Step/stool adjustable in height	
Printed informed consent forms	
Measuring tape and scale	
Tweezers, razer, alcohol, cotton pads	
Bench from KT + 2 low benches	
Pointer with markers (for manual displacement and circumference)	
Step	
Band from k2000	
25° decline board	
Metronome	
Video for prone flexion-extension movement	
Template for knee marker placement	

2. Before participant arrives

1. Take down cameras 7, 10, and 12 and place them on the ground under approximately 60 degrees
2. Open "Tringo Control Utility" → take out one EMG and push button
3. Open QTM → create project: **YEAR-MM-DD-MultiscaleModel-Mariska**
4. Settings → "input devices" → select "Delsys Trigno" and "Kistler"
5. Manually set the focus and aperture of cameras 7, 10, and 12
6. Settings → Camera System → "locate system" → check 2 camera groups → check each camera, remove white dots etc.
7. Calibration: place L-form wand on force plate (long arm = x-axis, short arm = y-axis)
8. Take T-form wand and click on "calibration" → move wand for 3 minutes → check volume
9. Calibrate force plates (see Operations Manual; make sure the equipment is as in setup **0**)

All steps above are done before participants arrive, then:

Ask participant to sign written consent	
Collect the age, length and weight of the participant	

Participant data

Number	**Age**	**Length**	**Weight**

3. Experimental set-up

Participant changes into shorts and shirt, no shoes or socks, nothing reflective.

3.1. <u>Small marker placement on dominant knee</u>

- Shave knee if needed
- Clean knee with alcohol
- Ask the participant to stretch and relax their leg. Gently push the patella proximally, then <u>draw a point (red)</u> on:
    - Base
- Ask the participant to bend their leg in 90 degrees and relax. Then palpate and <u>draw a point (red)</u> on:

    - Medial and lateral edges
    - Apex
- Draw the marker grid using the template by drawing (black) 49 points with a centre-to-centre distance of approximately 2.0 or 1.75 cm between each marker, starting from the palpated base (see figure). This grid will have 7 rows and 7 columns. Make sure most proximal row is not covering the patella. Also make sure the corner marker never covers the patella!
- Apply double-sided tape and place the markers.
- Make frontal and sagittal photos (extended and flexed).
- Measure and write down the approximate size of the patella:

Patellar length	**Patellar width**

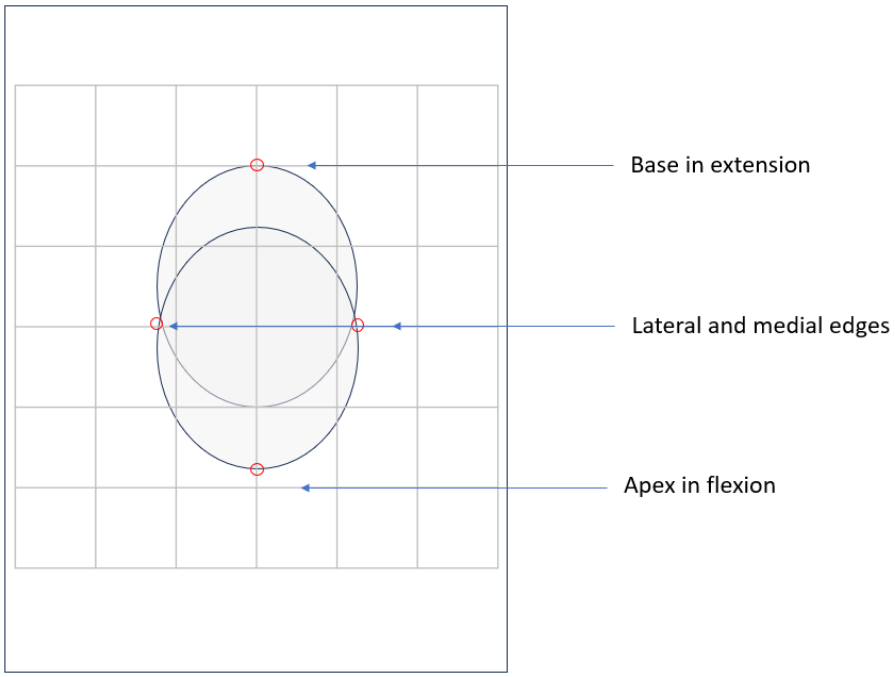

3.2. Normal marker placement

Next, 28 normal markers (12 mm) are placed on anatomical landmarks and 4 marker clusters are placed on leg segments:

- Draw a point for the LEC, MEC, and FEXTRA.

Segment	**Abbreviation**	**Landmark**
Foot	CaL	Calcaneus*
	Mt1	Metatarsal 1*
	Mt5	Metatarsal 5*

Tibia	LM	Lateral Malleolus*
	MM	Medial Malleolus*
	LTP	Lateral Tibia Plateau (or fibula head)*
	TC	Tibia Cluster*
Femur	LEC	Lateral Epicondyle*
	MEC	Medial Epicondyle*
	TM	Trochanter Major*
	FC	Femur cluster*
	FEXTRA	On the skin superior of LEC (only for dominant leg)
Pelvis	ASIS	Anterior Superior Iliac Spine*
	SAC	Sacrum
	PSIS	Posterior Superior Iliac Spine*
Torso	LumS	Lumbar Spine L4 (level of iliac crest)
	ThorS	Thoracic Spine T1 (C7 most prominent)
	Sho	Shoulder*

* indicates markers should be placed on both sides.

Take a picture of the subject with all markers.

3.3. EMG

Next, place the EMG on the muscles of the dominant leg. Shave hair and clean with alcohol. Write down the sensor number for each muscle

Muscle name	**Abbreviation**	**Sensor number**
Vastus lateralis	VL – sitting + slight flexion: 2/3 on the line from the anterior spina iliaca superior to the lateral side of the patella	
Rectus femoris	RF – sitting + slight flexion: In the direction of the line from the anterior spina iliaca superior to the superior part of the patella in direction of the line.	
Vastus medialis	VM – sitting + slight flexion: at 80% on the line between the anterior spina iliaca superior and the joint space in front of the	

	anterior border of the medial ligament almost perpendicular to the line.	
Biceps femoris	BF – flexed knee less than 90 deg + lateral rot tibia: 50% on the line between the ischial tuberosity and the lateral epicondyle of the tibia in direction of the line.	
Semitendinosus	SEM – flexed knee less than 90 deg + medial rot tibia: 50% on the line between the ischial tuberosity and the medial epicondyle of the tibia in direction of the line	
Tibialis anterior	TA – sitting: 1/3 on the line between the tip of the fibula and the tip of the medial malleolus in direction of the line	
Gastrocnemius lateral	GAL – extended knee: 1/3 of the line between the head of the fibula and the heel in direction of the line.	
Gastrocnemius medialis	GAM – extended knee: most prominent bulge of the muscle in direction of the leg	
Soleus	SOL – sitting 90 deg flexion: 2/3 of the line between the medial condyle of the femur to the medial malleolus in direction of the line.	

4. Motions

When all markers and sensors are placed, the measurements start. The participant will do all motions (barefoot). First practice every motion before measurement starts.

	Motion	**Duration**	**Duration QTM**	***Order***
1	**Calibration**			
1.1	Random motions	30 seconds	30 seconds	*1*
1.2	Static	5 seconds	5 seconds	*6*
2	**Maximal EMG determination**			
2.1	Hamstring activation	3 x	5 seconds	*11*
2.2	Power jump	3 x	5 seconds	*2*
3	**Patellar geometry determination**			
3.1	Static flexion	1 second	2 seconds	*3*
3.2	Circumference	1 x	20 seconds	*12*
4	**Motions of interest**			
4.1	Manual displacement	3x medial/lateral	10 seconds (for all 3)	*4*
4.2	Step-up	3 x	10 seconds	*5*
4.3	Single-leg decline squat	3 x	10 seconds	*7*
4.4	Single-leg squat with rotation	3 x	10 seconds	*8*
4.5	Supine flexion-extension	3 x 8 seconds	20 seconds	*10*
4.6	Prone flexion-extension	3 x 8 seconds	20 seconds	*9*

The flow of the measurements is as follows:

Make sure all equipment is placed as in setup **1**.

1.1 Random motions

For AIM model creation and to see if markers are detected by the system correctly.

2.1 Power jump

This is to activate the muscles (sub-)maximally. Ask participant to jump as high as possible, go all out.

4.1 Static flexion

This is to determine the geometry of the patella. The participant sits on the adjustable step with their ankle on the ground and their leg in an angle of 40-60°. Visually determine the angle for which the patella is most visible. Ask the participant to relax their leg and sit still during the measurement.

3.1 Manual displacement of the patella

Use the pointer with markers to manually displace the patella while the participant is sitting on the adjustable step with a relaxed leg. This is done to see how a known lateral displacement translates onto the marker mesh.

Be careful to not obstruct the view of the knee markers for the cameras!

3.2 Step-up

The participant starts with both feet on the floor. Then the participant steps up with one foot (of the NONDOMINANT knee) onto the step and continues with the other foot (of the DOMINANT knee) onto the step with force plate. Finish with placing the first foot on the step with the force plate as well.

Move all equipment to setup **2**.

1.2 Static

The marker locations in this body position will function as the reference pose as the markers are placed while the participant is standing still and minimal skin motion artifacts are seen here.

Start the measurement, then ask the participant to step on the force platform and stand still.

3.3 Single-leg decline squat

The participant starts with both feet on the floor. Then the participant steps up onto the 25° decline board on top of a force plate with their dominant foot and performs a slow, deep single-leg squat. A

finger can be used for stabilization, but make sure the upper body stays upright. The contralateral leg is kept forward during the squat.

3.4 Single-leg squat with rotation

The participant starts with both feet on the floor. Then the participant steps onto the force plate with their dominant foot and performs a slow single-leg squat with rotation. When standing on the right foot, the body turns towards the right, etc. A finger can be used for stabilization, but make sure the upper body stays upright. The contralateral leg is kept forward during the squat.

Move all equipment to setup **3**.

3.6 Prone flexion-extension

Remove both ASIS markers.

The participants lies on their belly on an elevated bench. The bench ends approximately 10 cm proximal to the knee joint line. The participant moves the DOMINANT knee from full extension to approximately 70° of flexion in 8 seconds. The NONDOMINANT knee is held in a fully flexed position. A video of the correct movement is shown and a metronome sound provided to guide the movement speed. The legs are held together by a rubber band.

Move all equipment to setup **4**.

3.5 Supine flexion-extension

Remove all markers on the back.

The participants lies on their back on a bench. The bench ends approximately 10 cm proximal to the knee joint line. The participant moves the DOMINANT knee from full extension to approximately 70° of flexion in 8 seconds, the NONDOMINANT foot is placed on the ground for support. A video of the correct movement is shown and a metronome sound provided to guide the movement speed. The legs are held together by a rubber band.

2.2 Hamstring activation

Participant prone on bench, holding the bench. Instructor pulls knee into extension and the participant tries to flex the knee maximally.

Move all equipment to setup **5**.

4.2 Circumference

This is to determine the circumference of the patella.

Remove the small markers from the knee, except for the corner markers.

The participant sits on a bench with their ankle on the ground and their leg in an angle of 40-60°. Visually determine the angle for which the patella is most visible. Ask the participant to relax their leg. During the measurement, slowly follow the circumference of the patella with the pointer with markers.

Appendix B. Description of additional OMC measurements

An additional 22 spherical retro-reflective markers (diameter 19 mm) were attached to anatomical landmarks of the legs, feet and torso, and 4 clusters of 3 markers on the thighs and shanks.

Next to the 3D positions of the retro-reflective markers, ground reaction force data was also measured three Kistler force plates (Kistler, Vienna, Austria). For participants 3, 4, and 5, muscle activity of nine muscles of the dominant leg was measured (Delsys Trigno Wireless EMG sensors, Delsys, Natick, USA), specifically vastus lateralis, vastus medialis, rectus femoris, biceps femoris, semitendinosus, tibialis anterior, gastrocnemius lateralis, gastrocnemius medialis, and soleus.

Additional to the EF movement, all participants also performed a step-up (SU), a single-leg decline squat (SLDS), and a single-leg squat with rotation (SLSR). The SU consisted of stepping onto an aerobics step with the nondominant leg and continuing the movement with the dominant leg onto a custom made step with two integrated force plates, one plate for each foot. For the SLDS, the participants placed the foot of their dominant leg onto a decline, stood upright until they found their balance, and then performed a single-leg squat. The SLSR consisted of a single-leg squat on the dominant leg, during which the upper body was externally rotated. To promote rotation, participants were encouraged to rotate their arms as far backwards as possible.

Furthermore, two passive measurements were performed, namely a manual displacement of the patella and a measurement of the circumference of the patella. For the manual displacement, the researcher translated the patella in medial-lateral direction using a custom-made pointer with three retro-reflective markers (diameter 14.5 mm). The dimensions of the pointer were known, allowing to compute the position of the tip of the pointer from the positions of the three markers. The circumference of the patella was measured by tracking the contour of the patella in a knee flexion for which the patella was prominent (around 60° - 80°) using the same custom-made pointer. For this, the marker grid on the knee was removed to avoid problems with the markers being on top of the contour.

Appendix C. Overview of the scripts used in all comparisons

Description of scripts for Geometry-Based 4D-CT

Table A1: All scripts used for processing the 4D-CT scans for Geometry-Based 4D-CT, including a description of what the script does, the input files needed and the output files generated by the script.

Script	**Description**	**Input**	**Output**
Segmentation_pt1.py	Performs the first part of the segmentation process (= identifying segments)	DICOM files	MRB-files per scan
Segmentation_pt2.py	Performs the second part of the segmentation process (= segment naming)	MRB-files per scan	○ MRB-files per scan ○ STL-files per bone per scan
Mesh_decimation.py	Decimates the meshes (reduces the number of faces and vertices) to speed up the rest of the scripts	STL-files per bone per scan	STL-files per bone per scan
Registration_femur_patella-Trimesh.py	Performs the registration of the static STL files on the dynamic STL files	STL-files per bone per scan	○ STL-files per bone per scan ○ Transformation matrices per bone per scan
Registrations_tibia_pt1-3Dslicer.py	Performs the first part of the tibia registration in which some deformation is allowed	STL-files per bone per scan	STL-files per bone per scan
Registrations_tibia_pt2-3Dslicer.py	Performs the second part of the tibia registration in which no deformation is allowed	STL-files per bone per scan	○ STL-files per bone per scan ○ Transformation matrices per bone per scan
Mesh_decimation_2.py	Decimates the meshes (reduces the number of faces and vertices) to speed up the rest of the scripts	STL-files per bone per scan	STL-files per bone per scan

ReRegistration.py	Performs registration of the static STL files on the result of the second part of the tibia registration	STL-files per bone per scan	○ STL-files per bone per scan ○ Transformation matrices per bone per scan
Transformation_femur_ align_NEW.py	Uses the transformation matrices of the registered femurs to make the patella and tibia move relative to a fixed femur, useful for making animations	○ STL-files per bone per scan ○ Transformation matrices of the registered femur per scan	STL-files per bone per scan
Coordinate_main_NEW.m	Computes the ACSs using the algorithm of Chen et al.	STL-files per bone per scan	○ ACS per bone per scan ○ Origins per bone ○ *DiagInfo per scan* ○ Optionally: Figures of STLs + ACSs
Compute_Kinematics_NEW.py	Computes PF and TF kinematics	ACS per bone per scan	○ PF kinematics ○ TF kinematics
Compute_Femur_ Kinematics.py	Computes global femur kinematics	Unaligned ACS of femur per scan	○ Global femur kinematics

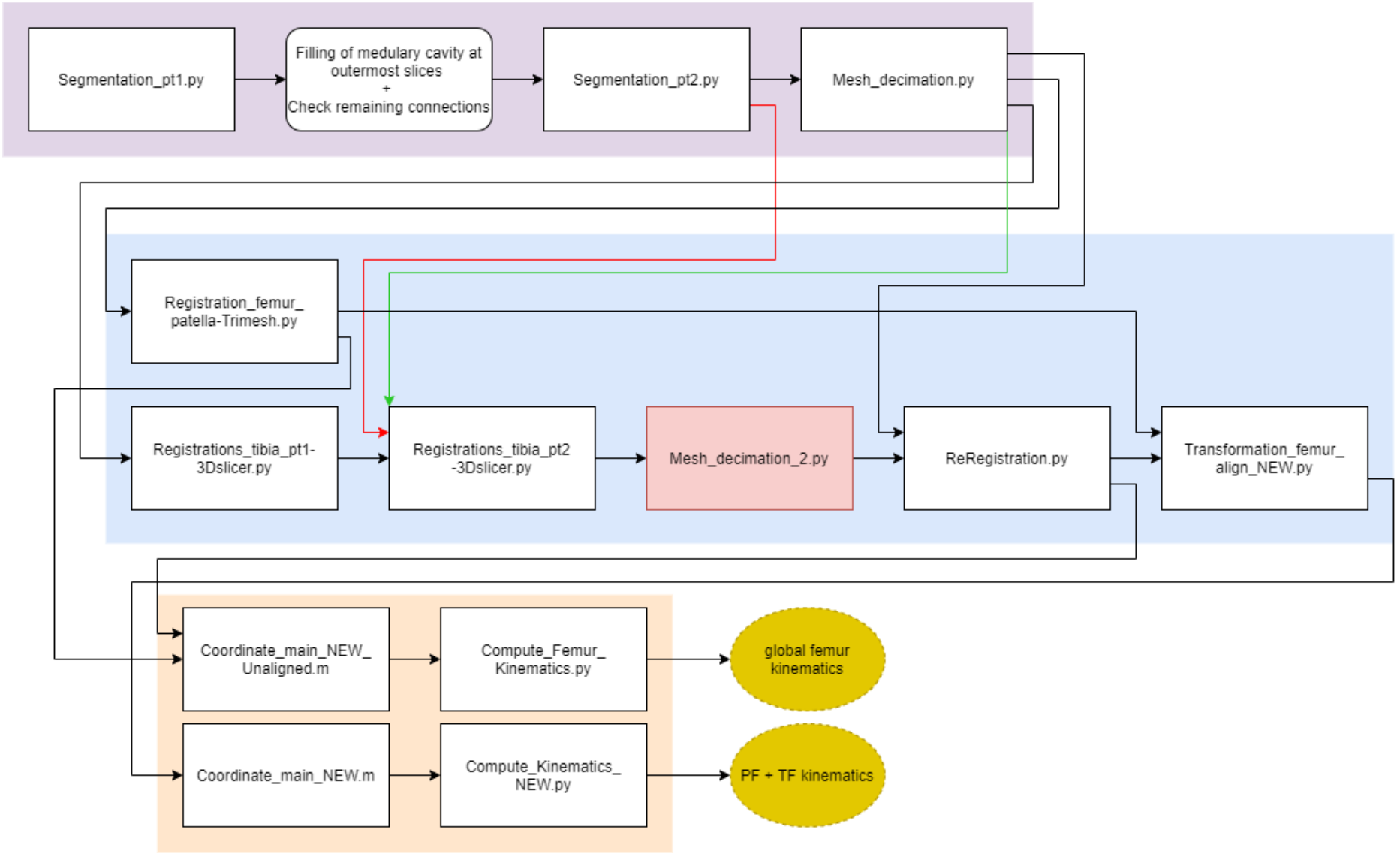

Figure S1: Workflow of all scripts used for processing the 4D-CT scans for Geometry-Based 4D-CT. The script indicated in red is probably unnecessary if the red line is replaced by the green line.

Description of scripts for Grid-Based 4D-CT

Table A 2: All scripts used for processing the 4D-CT scans for Grid-Based 4D-CT, including a description of what the script does, the input files needed and the output files generated by the script.

Script	**Description**	**Input**	**Output**
Segmentation_markers_pt1.py	Performs segmentation process	DICOM files	MRB-files per scan
MRB_2_STL.py	Transforms the MRB files to STL files	MRB-files per scan	○ STL files per marker per scan ○ CSV files per scan
Sphere_Fitting_ ManualNaming.py	Fits a sphere of given radius to each of the markers and outputs the centres of the spheres	○ STL files per marker per scan ○ CSV files per scan	○ ACS files per marker per scan ○ CSV files per scan
Register_Patella_to_Grid___ AND___ComputeACS_ ManualNaming.py	Interpolates the marker grid, registers a patella shape (mesh) onto this grid, and computes the ACS of the registered patella shape	○ CSV files of grid and femur markers per scan ○ STL file of patella mesh ○ ACS of patella mesh	○ STL files of fitted patella mesh per scan ○ Subfiles of registration process (TXT files of original, rotated, interpolated, and cropped grid, and STL files of pretransformed patella, pretransformed cut patella, fitted cut patella, and fitted full patella, costs of registration, virtual grid sizes) ○ ACS of fitted patella per scan ○ ACS of femur per scan, based on femur markers
Compute_Kinematics_ MarkerData_NOCHEN.py	Computes PF and TF kinematics using the femur and tibia ACS from the 4D-CT scans	○ ACS of fitted patella per scan ○ ACS of femur and tibia per scan (from Geometry-Based 4DCT)	○ PF kinematics ○ TF kinematics ○ Femur kinematics
Compute_Kinematics_ MarkerData_NOCHEN_ MarkerFemurACS.py	Computes PF and TF kinematics using the femur markers for the femur ACS and the tibia ACS from the 4D-CT scans	○ ACS of fitted patella per scan ○ ACS of femur per scan (from marker data) ○ ACS of tibia per scan (from Geometry-Based 4DCT)	○ PF kinematics ○ TF kinematics ○ Femur kinematics

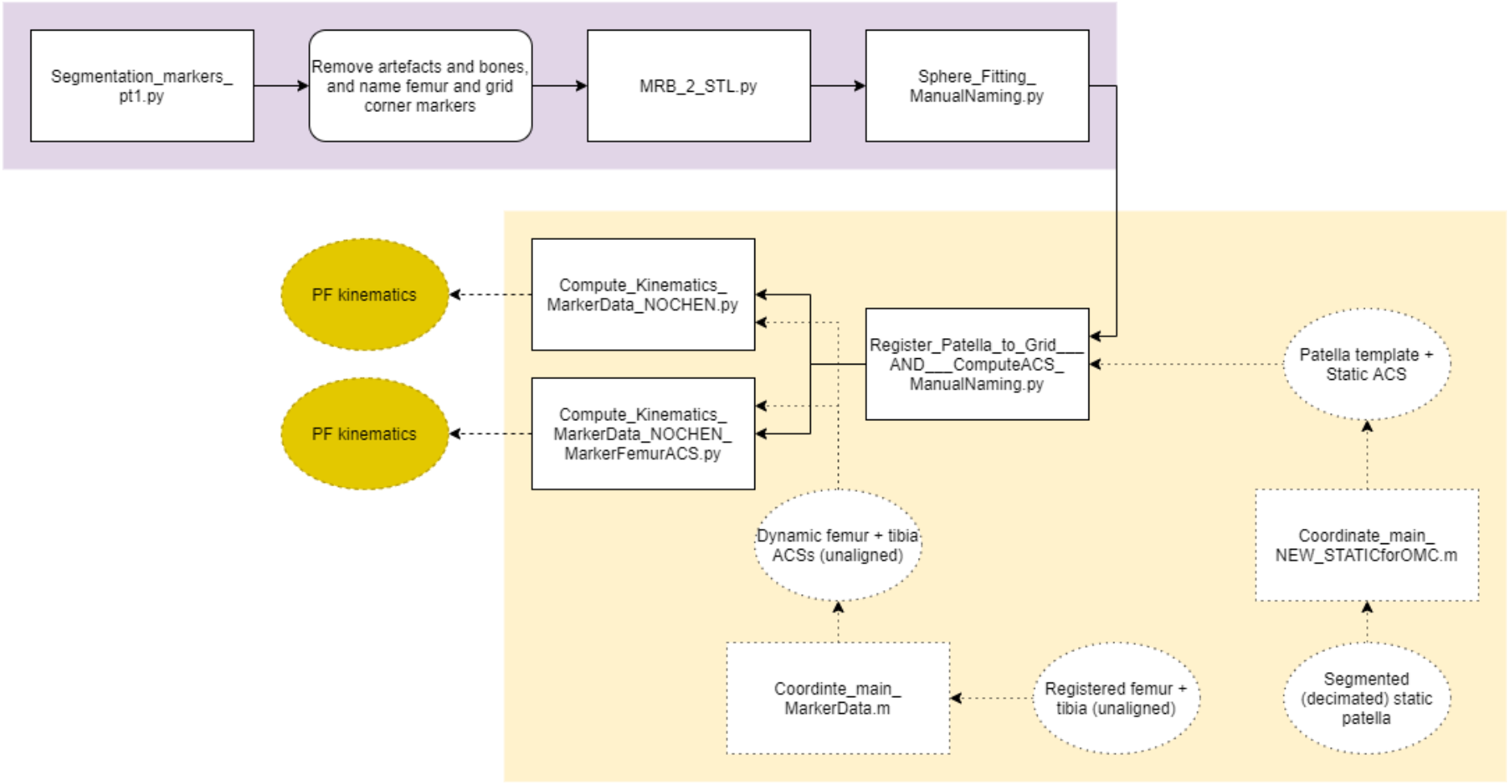

Figure S2: Workflow of all scripts used for processing the 4D-CT scans for Grid-Based 4D-CT. All dotted blocks and lines indicate scripts and data from the processing of Geometry-based 4D-CT.

Description of scripts for Marker-Based OMC

Table A3: All scripts used for processing the OMC data for Grid-Based OMC, including a description of what the script does, the input files needed and the output files generated by the script.

Script	**Description**	**Input**	**Output**
qtm2csv.m	Rewrites the QTM data to CSV files; also allows you to check for NAN values in the data	MAT files per measurement	CSV file with marker locations per measurement, per time step (set by step size)
Register_Patella_to_Grid_ OMC___AND___Compute_ Kinematics.py	Interpolates the marker grid, registers a patella shape (mesh) onto this grid, computes the ACS of the registered patella shape, and computes the femur and tibia ACS from the knee markers. Then computes PF and TF kinematics	○ CSV file with marker locations per measurement, per time step ○ STL file of patella mesh ○ ACS of patella mesh	○ STL files of fitted patella mesh per scan ○ Subfiles of registration process (TXT files of original, rotated, interpolated, and cropped grid, and STL files of pretransformed patella, pretransformed cut patella, fitted cut patella, and fitted full patella, costs of registration, virtual grid sizes) ○ PF kinematics ○ TF kinematics

Appendix D. Improvements made to the scripts for Geometry-based 4D-CT

Overall, a large issue with getting all scripts running, was that it was unclear which input files were needed for the scripts. Even using the figure with the workflow I could often hardly figure out which files to input. Therefore, updated the workflow figure, including all arrows for connections in data files. Furthermore, I named the folders in which data was saved after the script it was generated by. Moreover, I decided to leave the directions of my folders in the scripts to make it more clear for future users.

Segmentation_pt1.py

Most time spent on this script was due to an error (qMRMLSegmentEditorWidget::setMasterVolumeNode is deprecated, use setSourceVolumeNode method instead). It took some time to find out this was due to the 3DSlicer version that was used. This script does not work for newer versions of 3DSlicer than version 5.0.3.

Furthermore, the scans were numbered slightly differently than before, causing some problems with the numbering of the static scans.

Segmentation_pt2.py

I added parts handling the bed being visible during the 4D-CT scan. Previously, the script assumed only the tibia, femur, and patella of both legs were visible, causing wrong identification of the segments when the scanning bed was in the scanning window. Furthermore, there were errors with the numbering of the nodes, which I solved. Finally, I cleaned the code from some unnecessary parts.

Mesh_decimation.py

This script was added to decrease the file size of the segmentations. This was needed to speed up the scripts and to solve an error stating that not enough storage was available to run the registration scripts.

Registration_femur_patella-Trimesh.py

Since there was a difference in the numbering of the static scans, I changed the script so that it could handle these differences. Furthermore, I changed the location for saving to make the input/output connection between scripts more clear.

Registrations_tibia_pt1-3Dslicer.py

I again changed the script so that it could handle differences in the numbering of the static scans.

Registrations_tibia_pt2-3Dslicer.py

I again changed the script so that it could handle differences in the numbering of the static scans. I fixed an error with a bracket. I fixed an issue with a reference to a variable that did not exist. Finally, I changed the folders for loading and saving, because it was unclear where some output variables should be saved.

Mesh_decimation_2.py

This script was added to decrease the file size of the segmentations. However, I later realised that this script would not be needed if the decimated files are used in Registrations_tibia_pt2-3Dslicer instead of the non-decimated files.

ReRegistration.py

I fixed some issues with different naming styles used in this script. I again changed the script so that it could handle differences in the numbering of the static scans. I fixed an issue with the scan numbers that were different than in all other scripts.

Transformation_femur_align_NEW.py

I first tried to update this script by fixing issues. However, this script used .mat files as input files, but these files did not exist. After trying to fix this script for quite some time, I decided to start over and created a new script (based on the steps in the original script).

Coordinate_main_NEW.m

Based on some notes, I first updated this script to only compute the ACSs for the static scans. However, I later found out that the later scripts were not updated for this (although stated they were). Therefore, I created a new script (based on the original script) computing the ACSs for all dynamic scans. I also saved an issue of the script not correctly saving the locations of the origins.

Compute_Kinematics_NEW.py

I created this script from scratch because in the original files it was very unclear and confusing how the kinematics were computed.

Appendix E. Individual RMSE and r values

Individual Root Mean Square Errors (RMSEs) and Spearman correlation coefficients (r) for comparing Geometry-Based 4D-CT and Grid-Based 4D-CT

Table A4: Root mean square errors (RMSEs) for comparing Geometry-Based 4D-CT and Grid-Based 4D-CT, for all knee angles.

	P1	P2	P3	P4	P5
Spin (°)	22.5	22.6	33.4	24.3	29.4
Tilt (°)	23.0	9.4	22.2	14.6	16.7
Flexion (°)	14.9	23.8	10.0	8.2	11.2
AP translation (mm)	8.4	10.4	7.8	11.7	6.9
SI translation (mm)	12.6	15.8	9.0	1.5	9.0
ML translation (mm)	3.7	1.3	4.4	4.4	2.8

Table A5: Spearman correlation coefficients (r) for comparing Geometry-Based 4D-CT and Grid-Based 4D-CT, for all knee angles.

	P1	P2	P3	P4	P5
Spin (°)	-0.74	0.26	-0.91	-0.73	-0.72
Tilt (°)	0.18	-0.76	0.25	0	0.77
Flexion (°)	1	-0.61	0.99	0.90	0.99
AP translation (mm)	1	0.99	1	1	0.93
SI translation (mm)	1	0.83	1	1	0.87
ML translation (mm)	0.97	0.81	1	0.98	0.92

Table A6: Root mean square errors (RMSEs) for comparing Geometry-Based 4D-CT and Grid-Based 4D-CT, for the knee angles in which the patella is engaged (TF flexion > 20°).

	P1	P2	P3	P4	P5
Spin (°)	14.8	16.8	25	22.3	23.1
Tilt (°)	25.1	8.2	23.2	16.8	17.1
Flexion (°)	7.6	11.1	6.2	4.4	5.1
AP translation (mm)	7.7	10.1	6.5	11.8	7.0
SI translation (mm)	9.2	5.6	7.0	1.6	4.3
ML translation (mm)	3.6	1.2	4.4	4.3	2.8

Table A7: Spearman correlation coefficients (r) for comparing Geometry-Based 4D-CT and Grid-Based 4D-CT, for the knee angles in which the patella is engaged (TF flexion > 20°).

	P1	P2	P3	P4	P5
Spin (°)	-0.86	0.94	-0.95	-0.88	-0.97
Tilt (°)	0.4	0.54	0.3	0.21	0.98
Flexion (°)	1	1	0.98	1	1
AP translation (mm)	1	1	0.98	1	1
SI translation (mm)	1	1	1	1	1
ML translation (mm)	1	0.94	0.87	1	0.98

Individual Root Mean Square Errors (RMSEs) and Spearman correlation coefficients (r) for comparing Grid-Based OMC and Grid-Based 4D-CT

Table A8: Root mean square errors (RMSEs) for comparing Grid-Based OMC and Grid-Based 4D-CT, for all knee angles.

	P1	P2	P3	P4	P5
Spin (°)	6.7	8.5	5.2	3.5	5.7
Tilt (°)	3.8	4.0	4.0	1.6	8.1
Flexion (°)	7.9	6.5	9.4	10.3	8.5
AP translation (mm)	11.1	2.3	8.1	20.0	5.3
SI translation (mm)	11.9	38.7	12.1	14.0	8.8
ML translation (mm)	3.5	2.4	7.0	3.9	6.9

Table A9: Spearman correlation coefficients (r) for comparing Grid-Based OMC and Grid-Based 4D-CT, for all knee angles.

	P1	P2	P3	P4	P5
Spin (°)	0.22	0.95	0.98	0.93	0.99
Tilt (°)	0.04	0.53	-0.33	0.08	0.36
Flexion (°)	1	0.99	0.99	0.92	0.98
AP translation (mm)	-0.63	0.92	-0.65	0.44	-0.70
SI translation (mm)	1	0.99	0.99	0.93	0.89
ML translation (mm)	0.76	0.53	-0.24	0.76	0.82

Table A10: Root mean square errors (RMSEs) for comparing Grid-Based OMC and Grid-Based 4D-CT, for the knee angles in which the patella is engaged (TF flexion > 20°).

	P1	P2	P3	P4	P5
Spin (°)	7.8	6.7	4.6	3.5	7
Tilt (°)	4	3.6	1.5	1.4	5.3
Flexion (°)	8.5	6.4	10.4	11.1	10.2
AP translation (mm)	14.5	2.1	9.2	21.3	5.7
SI translation (mm)	12.3	40.2	13.1	14	10.4
ML translation (mm)	2.9	1.6	4.2	4.1	6.1

Table A11: Spearman correlation coefficients (r) for comparing Grid-Based OMC and Grid-Based 4D-CT, for the knee angles in which the patella is engaged (TF flexion > 20°).

	P1	P2	P3	P4	P5
Spin (°)	-0.89	0.90	0.91	0.90	0.97
Tilt (°)	-0.43	0.57	0.59	-0.05	0.92
Flexion (°)	1	0.98	0.97	0.87	0.90
AP translation (mm)	0.60	0.93	0.36	0.85	-0.80
SI translation (mm)	1	1	0.98	0.88	1
ML translation (mm)	0.94	0.14	-0.1	0.66	0.98

Appendix F. Additional Results

Geometry-Based 4D-CT vs. Grid-Based 4D-CT excluding participant 2

The PF kinematics for participant 1, 3, 4, and 5 can be found in Figure A1.

The average RMSEs were similar to those including participant 2, both for all knee angles, and for the knee angles in which the patella is engaged (Table A12). When excluding participant 2, the average correlation for flexion increased from moderate to very high for all knee angles. Furthermore, the correlation for spin for the engaged knee angles changed from moderate negative to very high negative.

When excluding participant 2, most data still fell within the limits of agreement of the Bland-Altman plot for the comparison of *Geometry-Based 4D-CT* and *Grid-Based 4D-CT*, both for all TF flexion angles (Figure A2) and for the TF flexion angles in which the patella is engaged (Figure A3). For spin, flexion/extension, and ML translation, the points were approximately on a straight sloped line per participant.

Table A12: Average root mean square errors (RMSEs) and Spearman correlation coefficients (r), over participant 1, 3, 4, and 5, for comparing Geometry-Based 4D-CT and Grid-Based 4D-CT, for all knee angle, and for the knee angles in which the patella is engaged (TF flexion > 20°).

	RMSE	**RMSE - Engaged**	**r**	**r - Engaged**
Spin (°)	27.4	21.3	-0.78	-0.91
Tilt (°)	19.1	20.6	0.19	0.48
Flexion (°)	11.1	5.8	1	1
AP translation (mm)	8.7	8.3	0.98	1
SI translation (mm)	8.0	5.5	0.97	1
ML translation (mm)	3.8	3.8	0.97	0.96

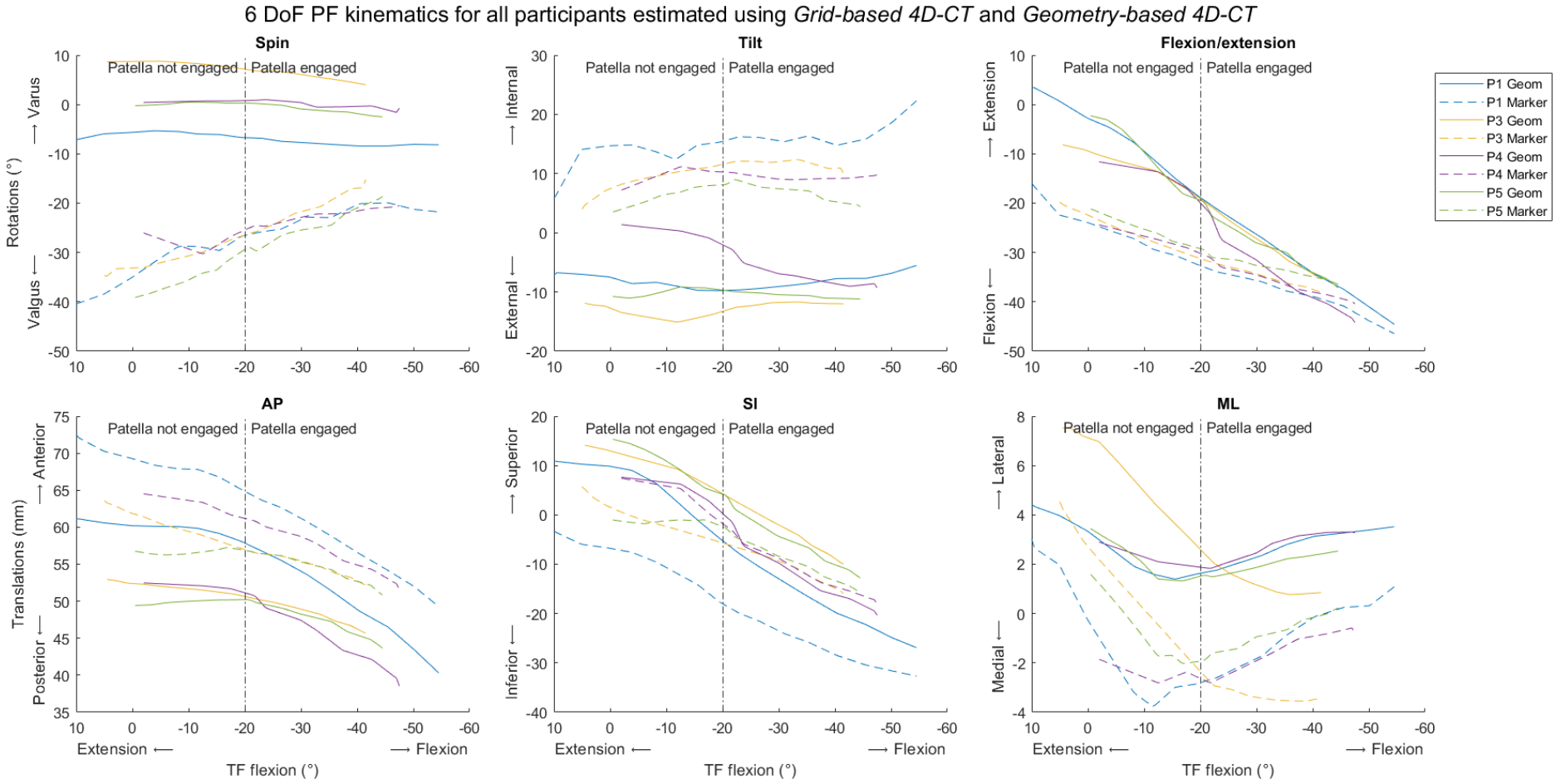

Figure A1: PF kinematics of participant 1, 3, 4, and 5 for Geometry-Based 4D-CT vs. Grid-Based 4D-CT. TF flexion angle is computed from tibial and femoral geometry for both methods. Each colour represents a different participant.

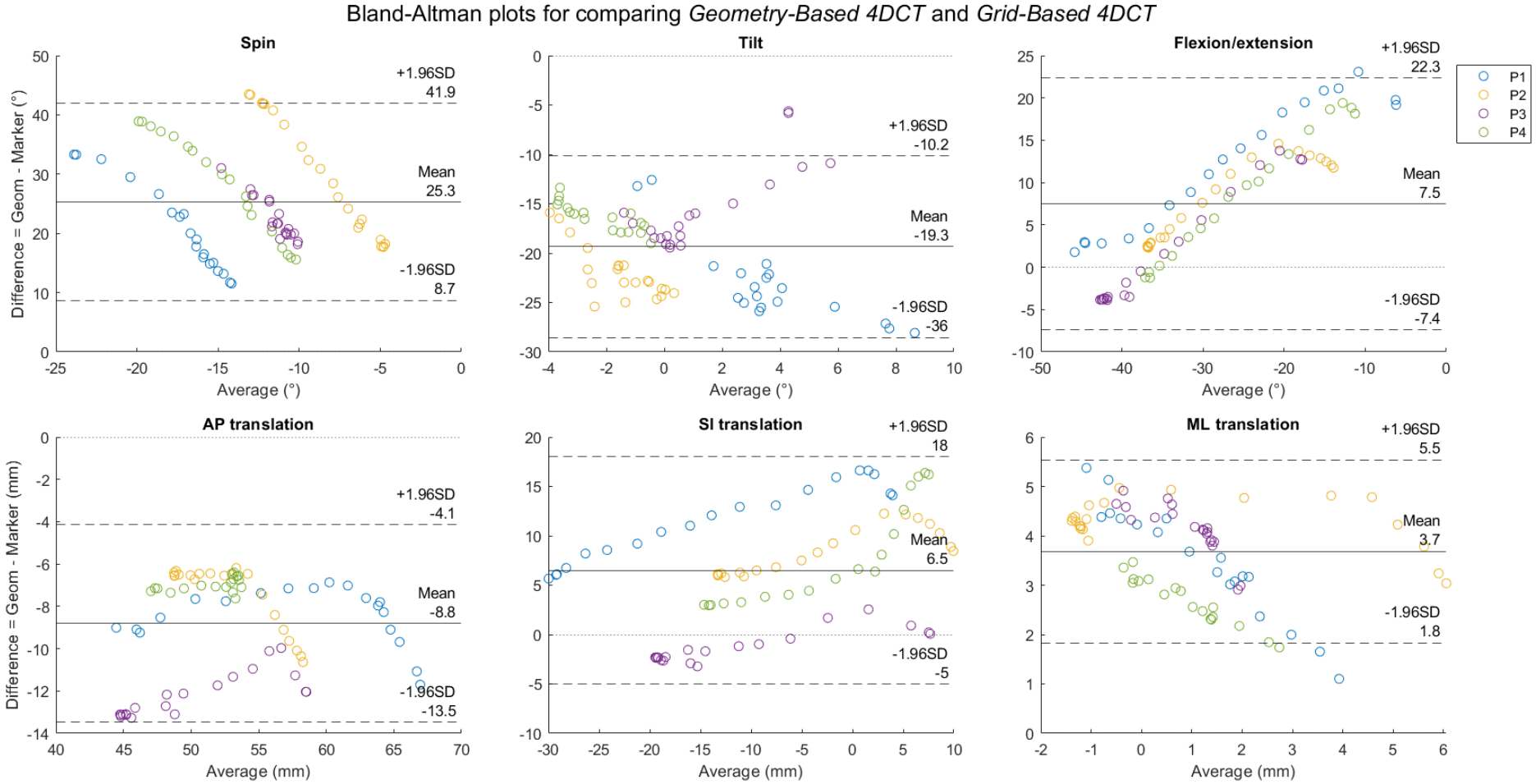

Figure A2: Bland-Altman plots for participant 1, 3, 4, and 5 for comparing Geometry-Based 4D-CT and Grid-Based 4D-CT, for all knee angles. Mean and difference were computed for each TF angle for which grid markers could be segmented, causing a different amount of data points per participant. Each colour represents a different participant.

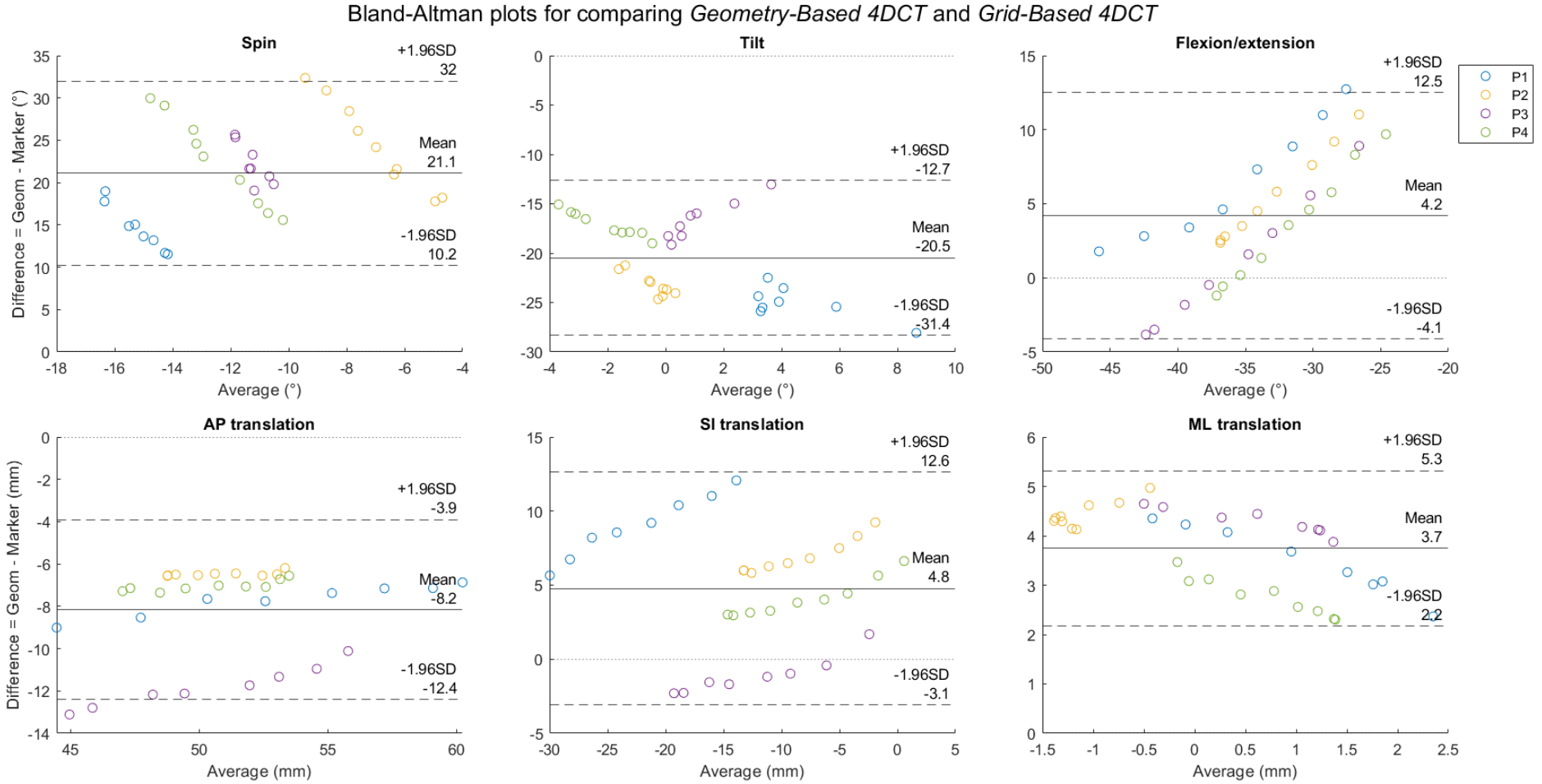

Figure A3: Bland-Altman plots for participant 1, 3, 4, and 5 for comparing Geometry-Based 4D-CT and Grid-Based 4D-CT, for the knee angles in which the patella is engaged (TF flexion > 20°). Mean and difference were computed for each TF angle for which grid markers could be segmented, causing a different amount of data points per participant. Each colour represents a different participant.

Geometry-Based 4D-CT vs. Grid-Based 4D-CT for using the result of the previous TF flexion angle as initial guess in the ICP

The total cost was similar or slightly lower for all participants, yet the pattern of the cost over the TF flexion angle was the same as for the ICP without coupled initial guess (Figure A4). The largest differences in PF kinematics when comparing to not using the coupled initial guess were in spin and tilt (Figure A5). The results for participant 2 were closer to the other 4 participants, and even closer to Geometry-Based 4D-CT as well.

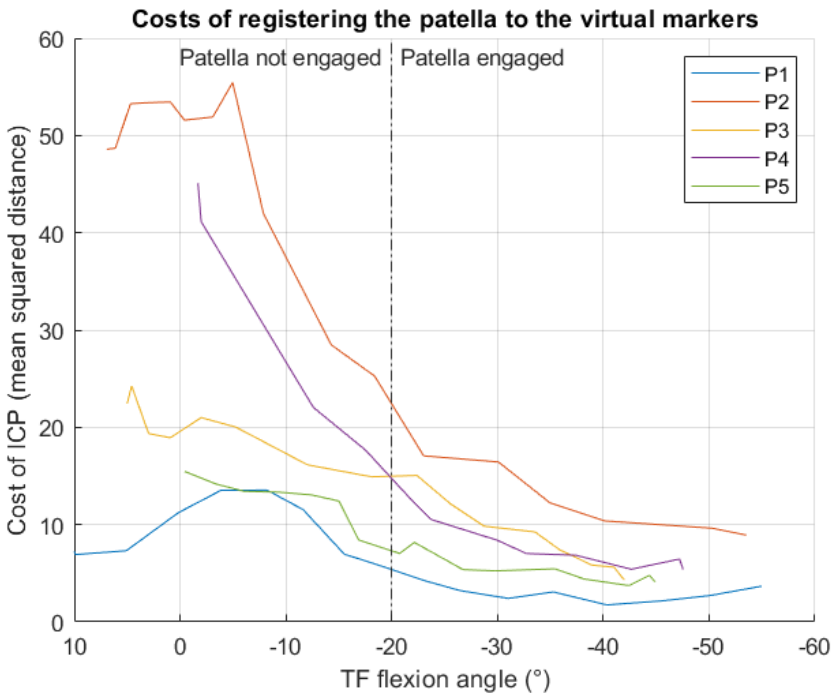

Figure A4: Cost in the last step of the ICP algorithm when using a coupled initial guess for each TF flexion angle. The cost is computed as the mean squared distance of the points on the patella mesh to the selected virtual grid markers. The cost is plotted against the TF flexion angle, which is computed using the tibial and femoral geometry. Each colour represents a different participant.

The RMSE angles generally decreased for rotations and increased or were similar for translations when compared to not using the coupled initial guess, both for all TF angles and for the TF angles in which the patella is engaged (Table A13, Table A15). Correlations improved for flexion for all TF angles, but decreased for ML translation for all TF angles and for the TF angles in which the patella is engaged (Table A14, Table A16).

Table A13: Root mean square errors (RMSEs) for comparing Geometry-Based 4D-CT and Grid-Based 4D-CT using a coupled initial guess, for all knee angles.

	P1	P2	P3	P4	P5	Mean
Spin (°)	15.7	2.9	7.6	18.5	16.6	12.3
Tilt (°)	20.5	4.7	11.2	13.2	11.1	12.1
Flexion (°)	14.0	20.0	7.9	6.3	8.4	11.3
AP translation (mm)	15.1	20.7	12.4	14.2	10.5	14.6
SI translation (mm)	14.4	15.4	9.1	4.4	10.0	10.7
ML translation (mm)	2.7	2.6	3.2	4.7	2.3	3.1

Table A14: Spearman correlation coefficients (r) for comparing Geometry-Based 4D-CT and Grid-Based 4D-CT using a coupled initial guess, for all knee angles.

	P1	P2	P3	P4	P5	Mean
Spin (°)	-0.59	0.11	-0.85	0.63	0.68	0
Tilt (°)	-0.24	0.50	0.27	-0.95	-0.39	-0.16
Flexion (°)	1	1	1	1	1	1
AP translation (mm)	1	1	1	1	0.71	0.94
SI translation (mm)	1	0.98	1	0.98	1	0.99
ML translation (mm)	0.25	0.94	0.95	0.84	0.06	0.61

Table A15: Root mean square errors (RMSEs) for comparing Geometry-Based 4D-CT and Grid-Based 4D-CT using a coupled initial guess, for the knee angles in which the patella is engaged (TF flexion > 20°).

	P1	P2	P3	P4	P5	Mean
Spin (°)	10.1	4.3	4.9	19.1	17.9	11.2
Tilt (°)	22.6	5.1	12.3	15.9	13.9	14.0
Flexion (°)	7.4	9.0	4.7	3.2	3.4	5.5
AP translation (mm)	7.3	8.6	4.6	11.3	5.8	7.5
SI translation (mm)	9.7	8.5	6.7	3.3	5.5	6.7
ML translation (mm)	3.0	2.6	4.1	4.6	1.2	3.1

Table A16: Spearman correlation coefficients (r) for comparing Geometry-Based 4D-CT and Grid-Based 4D-CT using a coupled initial guess, for the knee angles in which the patella is engaged (TF flexion > 20°).

	P1	P2	P3	P4	P5	Mean
Spin (°)	-0.52	-0.26	-0.37	0.67	0.62	0.03
Tilt (°)	0.26	-0.43	0.47	-0.86	-0.82	-0.27
Flexion (°)	1	1	0.98	1	1	1
AP translation (mm)	1	1	0.98	1	1	1
SI translation (mm)	1	0.94	1	1	1	0.99
ML translation (mm)	-0.31	0.94	0.68	0.88	-0.83	0.27

Most data fell within the limits of agreement of the Bland-Altman plot for the comparison of *Geometry-Based 4D-CT* and *Grid-Based 4D-CT* with coupled initial guess, both for all TF flexion angles (Figure A6) and for the TF flexion angles in which the patella is engaged (Figure A7). The data falling outside of the limits of agreement, mostly belonged to participant 2. For flexion/extension and SI translation, the points were approximately on a straight sloped line per participant.

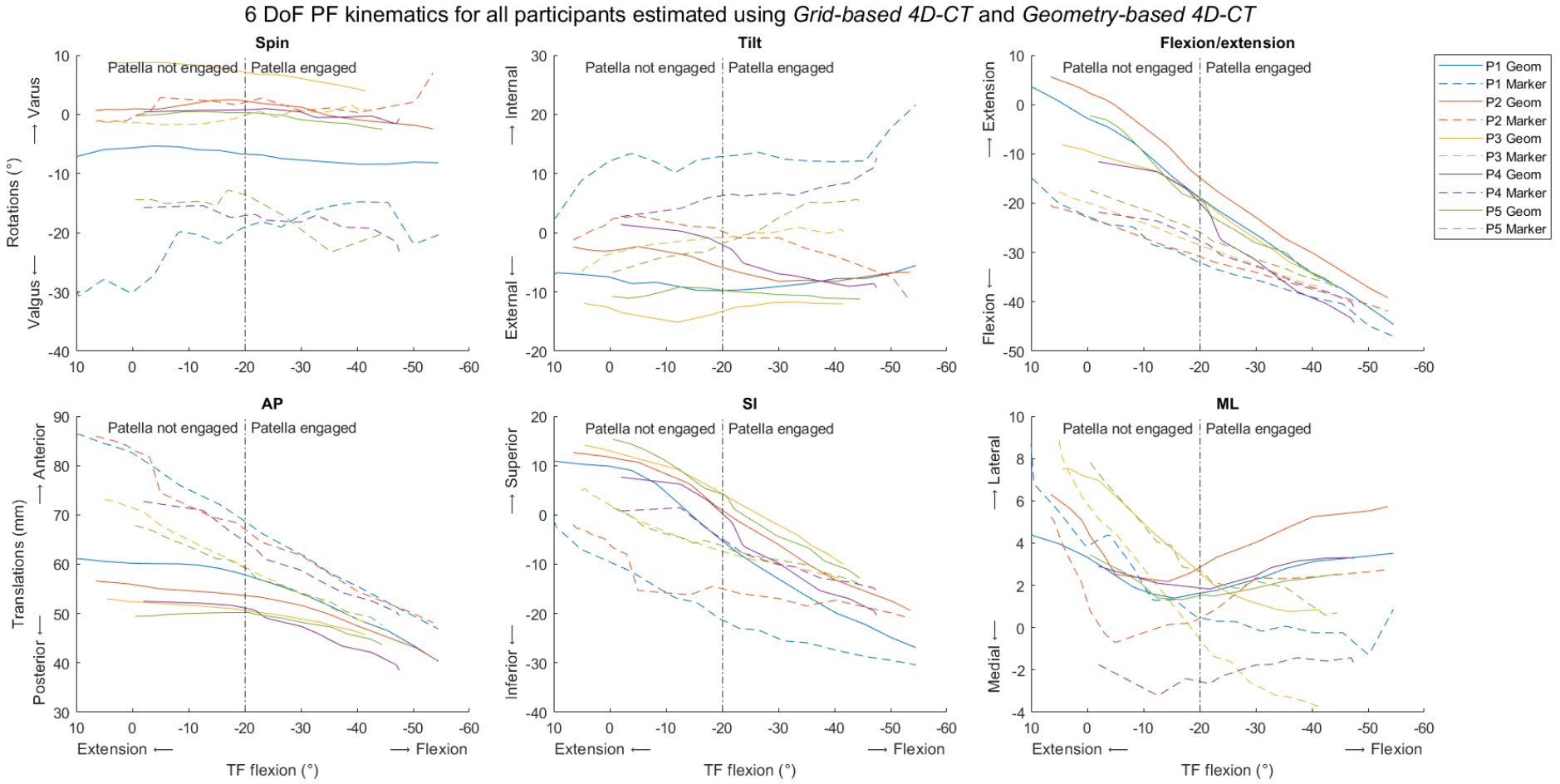

Figure A5: PF kinematics of all participants for Geometry-Based 4D-CT vs. Grid-Based 4D-CT with coupled initial guess. TF flexion angle is computed from tibial and femoral geometry for both methods. Each colour represents a different participant.

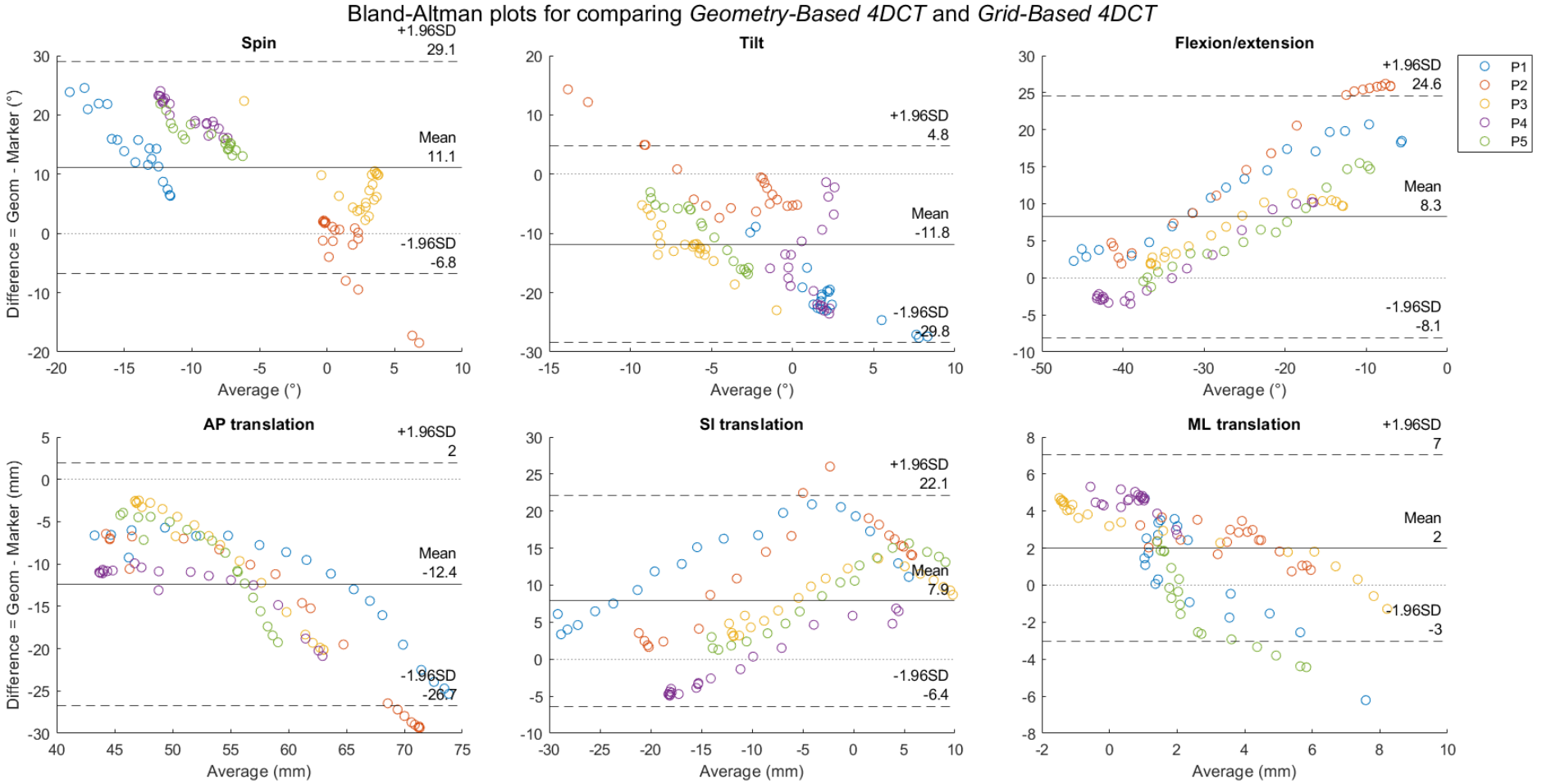

Figure A6: Bland-Altman plots for comparing Geometry-Based 4D-CT and Grid-Based 4D-CT with coupled initial guess, for all knee angles. Mean and difference were computed for each TF angle for which grid markers could be segmented, causing a different amount of data points per participant. Each colour represents a different participant.

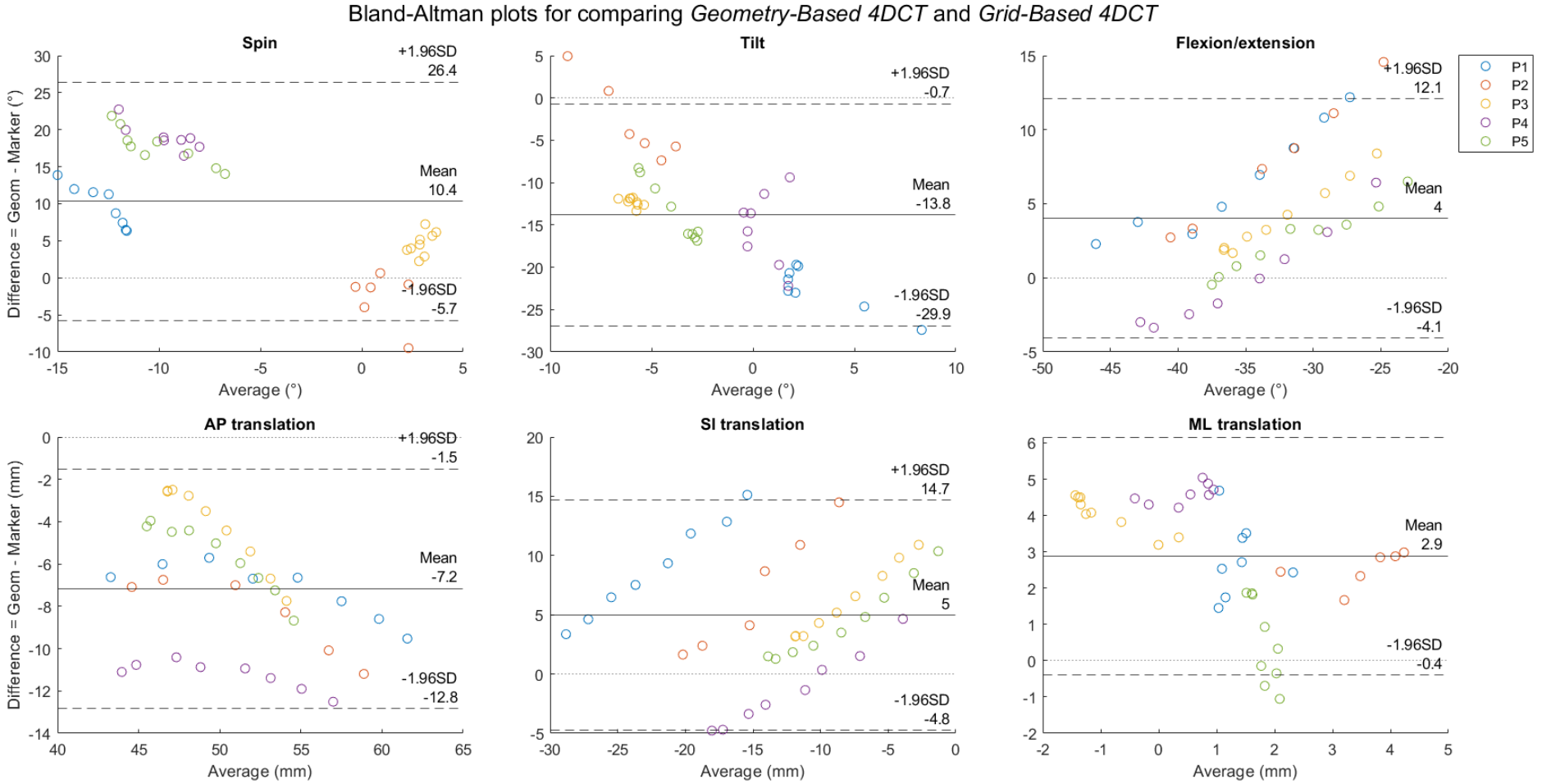

Figure A7: Bland-Altman plots for comparing Geometry-Based 4D-CT and Grid-Based 4D-CT with coupled initial guess, for the knee angles in which the patella is engaged (TF flexion > 20°). Mean and difference were computed for each TF angle for which grid markers could be segmented, causing a different amount of data points per participant. Each colour represents a different participant.

Grid-Based 4D-CT vs. Grid-Based OMC excluding participant 2

The PF kinematics for participant 1, 3, 4, and 5 can be found in Figure A8.

The average RMSEs were similar to those including participant 2, both for all knee angles and for the knee angles in which the patella is engaged. However, for SI translation, the RMSE was smaller when excluding participant 2 (Table A17). Correlations were similar when excluding participant 2, although the correlation for AP translation became moderate negative and low instead of low negative and moderate, for respectively all TF angles and the engaged TF angles.

When excluding participant 2, most data still fell within the limits of agreement of the Bland-Altman plot for the comparison of *Grid-Based OMC* and *Grid-Based 4D-CT*, both for all TF flexion angles (Figure A9) and for the TF flexion angles in which the patella is engaged (Figure A10). There still was a distinction between participants 3 and 5, and participants 1, and 4 for ML translation and AP translation. Data did not seem to be on a straight sloped line.

Table A17: Average root mean square errors (RMSEs) and Spearman correlation coefficients (r), over participant 1, 3, 4, and 5, for comparing Grid-Based OMC and Grid-Based 4D-CT, for all knee angle, and for the knee angles in which the patella is engaged (TF flexion > 20°).

	RMSE	**RMSE - Engaged**	**r**	**r - Engaged**
Spin (°)	5.2	5.7	0.78	0.47
Tilt (°)	4.4	3.1	0.04	0.26
Flexion (°)	9.0	10.0	0.97	0.93
AP translation (mm)	11.2	12.7	-0.39	0.25
SI translation (mm)	11.7	12.4	0.95	0.96
ML translation (mm)	5.3	4.3	0.53	0.62

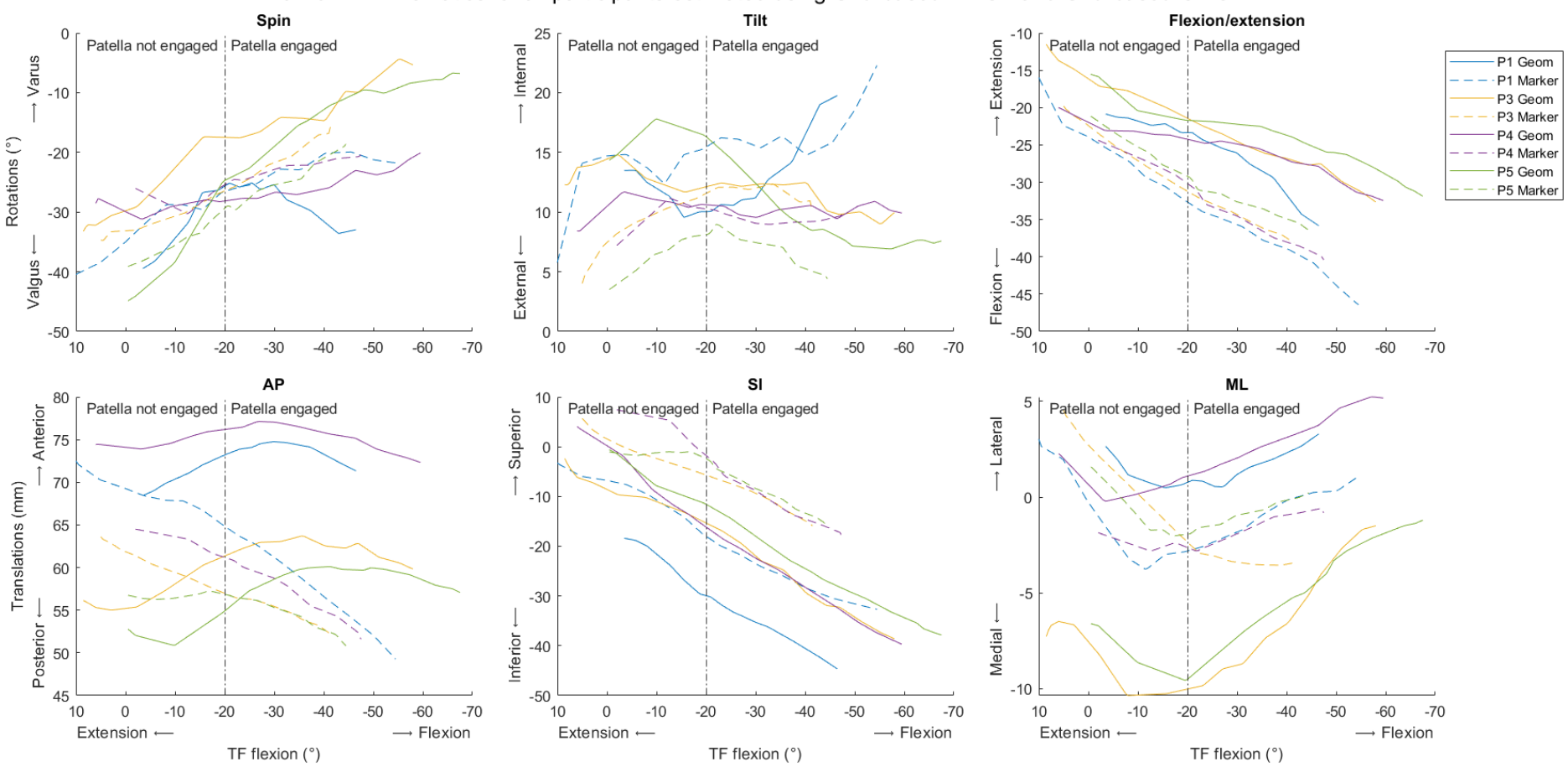

Figure A8: PF kinematics of participant 1, 3, 4, and 5 for Geometry-Based 4D-CT vs. Grid-Based 4D-CT. TF flexion angle is computed from tibial and femoral geometry for Grid-based 4D-CT and from tibia and femur markers for Grid-based OMC. Each colour represents a different participant.

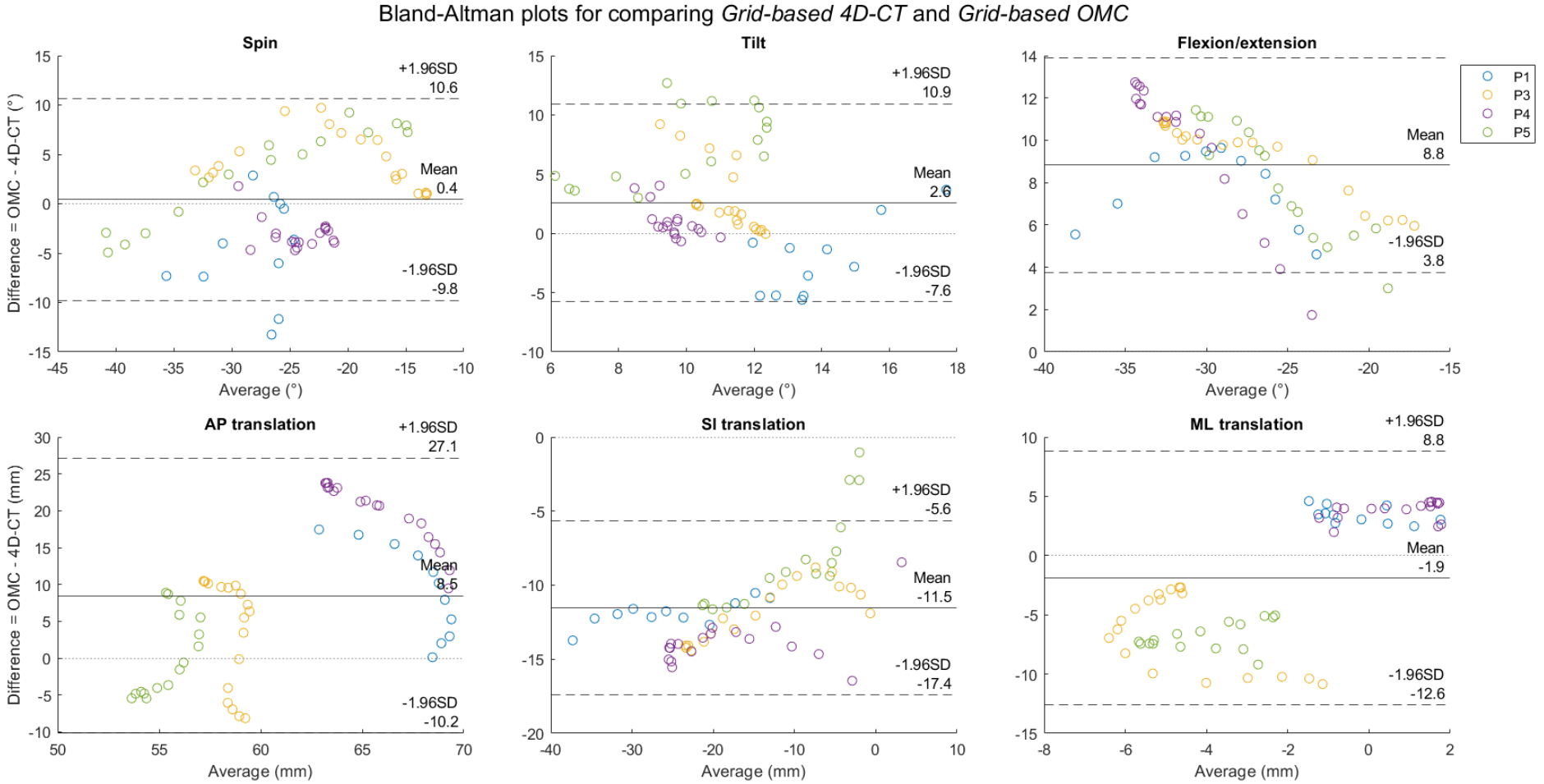

Figure A9: Bland-Altman plots for participant 1, 3, 4, and 5 for comparing Grid-Based OMC and Grid-Based 4D-CT, for all knee angles. Mean and difference were computed for each TF angle for which grid markers could be segmented, causing a different amount of data points per participant. Each colour represents a different participant.

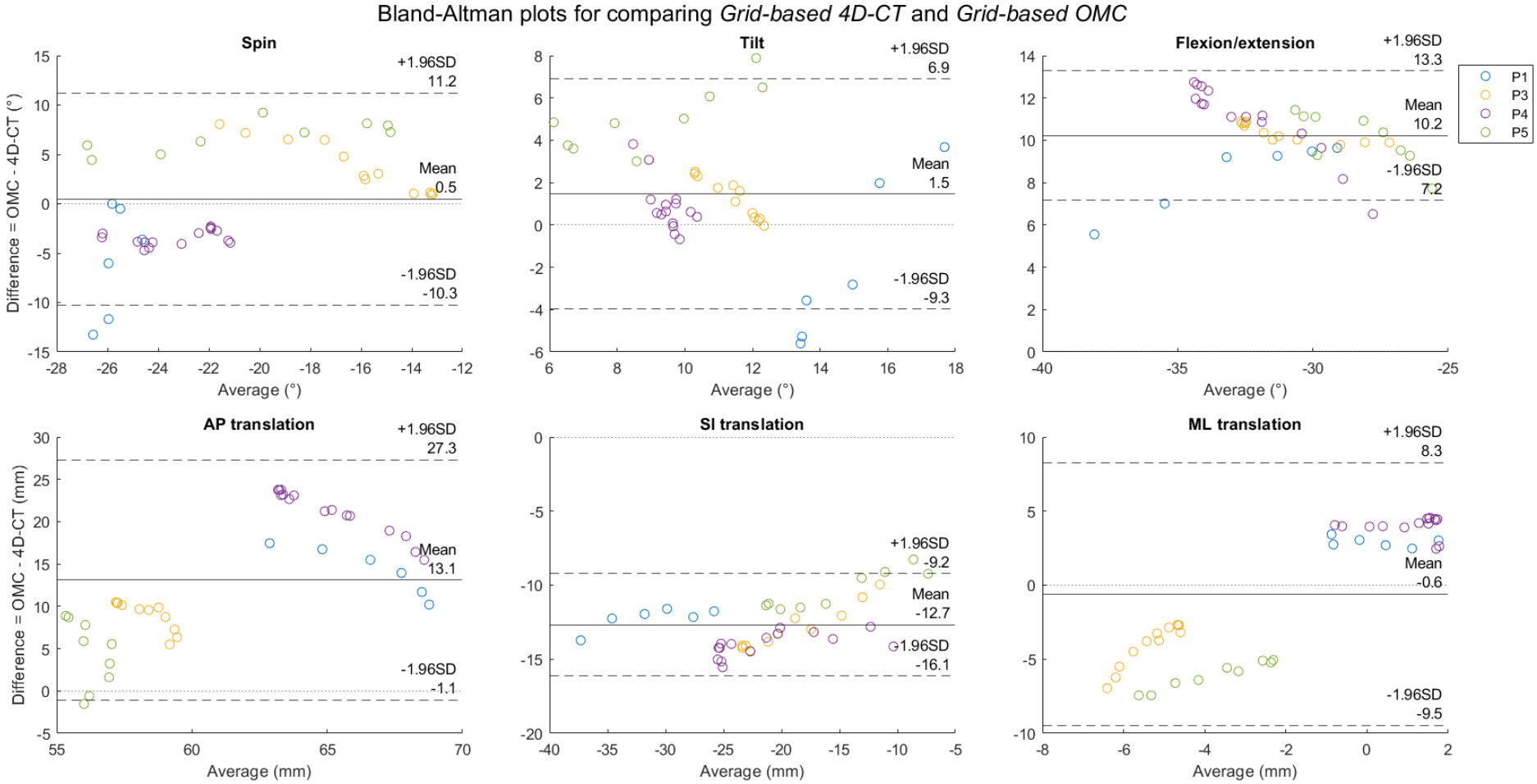

Figure A10: Bland-Altman plots for participant 1, 3, 4, and 5 for comparing Grid-Based OMC and Grid-Based 4D-CT, for the knee angles in which the patella is engaged (TF flexion > 20°). Mean and difference were computed for each TF angle for which grid markers could be segmented, causing a different amount of data points per participant. Each colour represents a different participant.